ACS Pharmacology & Translational Science

pubs.acs.org/ptsci

Article

Innate Immunity Plays a Key Role in Controlling Viral Load in COVID-19: Mechanistic Insights from a Whole-Body Infection Dynamics Model

Prashant Dogra,* Javier Ruiz-Ramírez,& Kavya Sinha,& Joseph D. Butner,& Maria J. Peláez, Manmeet Rawat, Venkata K. Yellepeddi, Renata Pasqualini, Wadih Arap, H. Dirk Sostman, Vittorio Cristini, and Zhihui Wang*

Cite This: *ACS Pharmacol. Transl. Sci.* 2021, 4, 248−265

Read Online

ACCESS | Metrics & More | Article Recommendations | Supporting Information

ABSTRACT: Severe acute respiratory syndrome coronavirus 2 (SARS-CoV-2) is a pathogen of immense public health concern. Efforts to control the disease have only proven mildly successful, and the disease will likely continue to cause excessive fatalities until effective preventative measures (such as a vaccine) are developed. To develop disease management strategies, a better understanding of SARS-CoV-2 pathogenesis and population susceptibility to infection are needed. To this end, mathematical modeling can provide a robust *in silico* tool to understand COVID-19 pathophysiology and the *in vivo* dynamics of SARS-CoV-2. Guided by ACE2-tropism (ACE2 receptor dependency for infection) of the virus and by incorporating cellular-scale viral dynamics and innate and adaptive immune responses, we have developed a multiscale mechanistic model for simulating the time-dependent evolution of viral load distribution in susceptible organs of the body (respiratory tract, gut, liver, spleen, heart, kidneys, and brain). Following parameter quantification with *in vivo* and clinical data, we used the model to simulate viral load progression in a virtual patient with varying degrees of compromised immune status. Further, we ranked model parameters through sensitivity analysis for their significance in governing clearance of viral load to understand the effects of physiological factors and underlying conditions on viral load dynamics. Antiviral drug therapy, interferon therapy, and their combination were simulated to study the effects on viral load kinetics of SARS-CoV-2. The model revealed the dominant role of innate immunity (specifically interferons and resident macrophages) in controlling viral load, and the importance of timing when initiating therapy after infection.

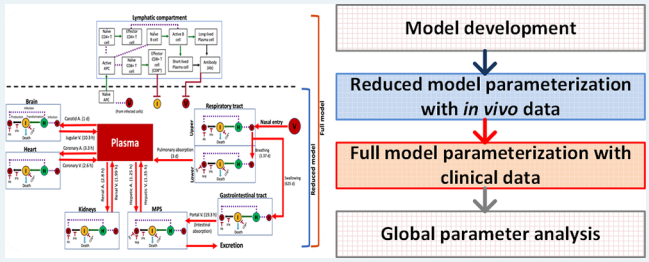

KEYWORDS: *COVID-19, in silico clinical trials, mathematical modeling, pharmacokinetics, SARS-CoV-2, viral dynamics*

In January 2020, severe acute respiratory syndrome coronavirus 2 (SARS-CoV-2) was identified as the infectious agent causing an outbreak of viral pneumonia in Wuhan, China. It was soon established that droplet-based human to human transmission was occurring, and on March 11, 2020, the World Health Organization characterized coronavirus disease 2019 (COVID-19) as a pandemic. As of December 25, 2020, COVID-19 has infected more than 79 million people and caused more than 1.74 million deaths worldwide.[1] A pandemic-scale outbreak creates tremendous socioeconomic burden due to thwarted productivity, a spike in healthcare expenses, and irreparable loss of human lives.[2,3] Furthermore, implementation of social and physical isolation measures has caused many countries to declare states of emergency and lockdowns with border closures.

SARS-CoV-2 is the seventh identified human coronavirus and the third novel one to emerge in the last 20 years. It has a single-stranded positive sense RNA genome of about 30,000 nucleotides that encodes ∼27 proteins including 4 structural proteins. A surface-expressed spike protein mediates receptor binding and membrane fusion with host cells, and the virus interacts with the angiotensin converting enzyme 2 (ACE2) receptor to gain entry into cells.[4] ACE2 mRNA is present in almost all human organs, but the receptor is particularly highly expressed on the surface of lung alveolar epithelial cells and enterocytes of the small intestine, thereby allowing a preferential accumulation of the virus in these organs.[5] The incubation period of SARS-CoV-2 ranges from about 3−17 days, and COVID-19 diagnosis cannot be made based on symptoms alone, as most are nonspecific and may be confused for more common ailments. The more serious sequelae of

Received: October 30, 2020
Published: December 30, 2020

https://dx.doi.org/10.1021/acsptsci.0c00183
ACS Pharmacol. Transl. Sci. 2021, 4, 248−265

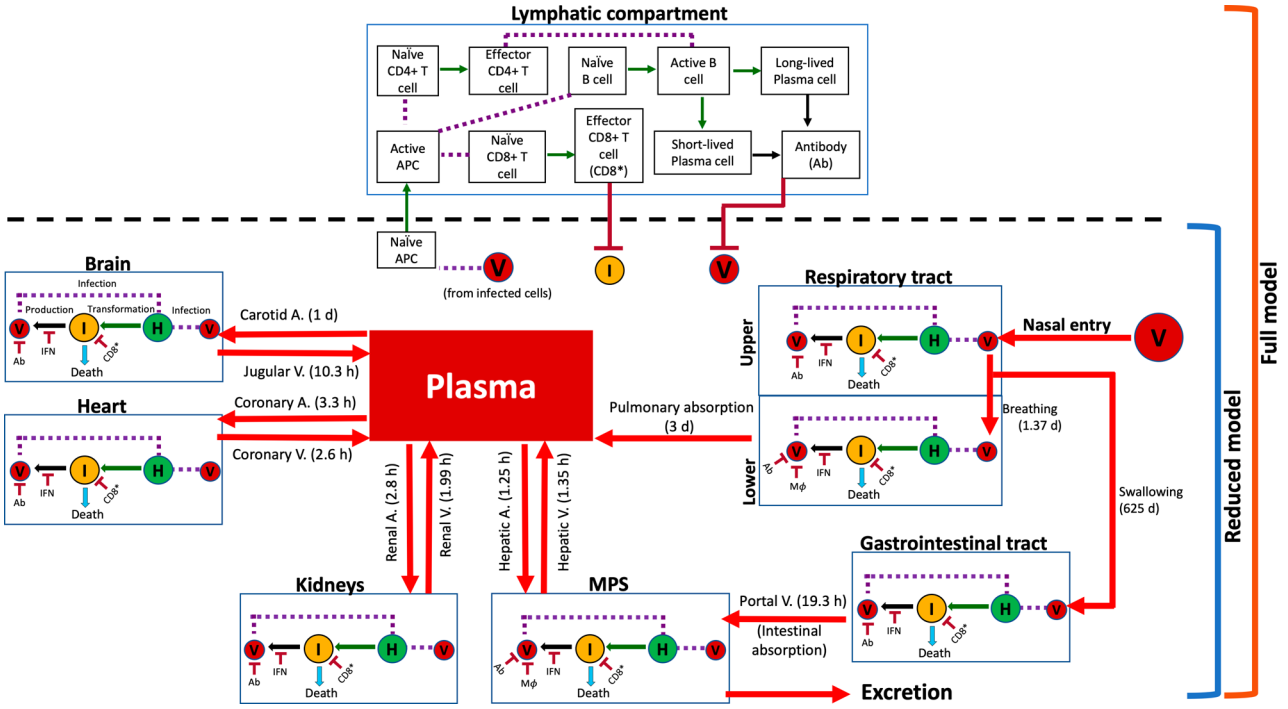

Figure 1. Model schematic showing system interactions. Connectivity diagram between compartments indicating viral transport mechanisms, cell populations, immune system agents, and their interactions. Estimated characteristic times of the various transport processes are given in parentheses alongside red arrows. Notation: (V) virus, (H) healthy cells, (I) infected cells, (IFN) interferon, (Ab) antibody, (CD8*) effector $CD8^+$ cells, and (APC) antigen presenting cells. Solid red arrows indicate transport of virus; solid green arrows indicate transformation of a cell into another type; solid black arrows indicate production of an agent; purple dashed lines indicate interaction between two agents; and solid dark red arrows with a flat head indicate inhibition. MPS stands for mononuclear phagocytic system and comprises liver and spleen.

infection includes acute respiratory distress syndrome (ARDS) and sepsis caused by the cytokine storm from the immune response to infection, which is believed to be the leading cause of mortality in COVID-19 patients.[6] Screening for COVID-19 is done via nucleic acid testing by RT-PCR (specimens from both upper and lower respiratory tracts) and pulmonary CT scans. The viral load in naso- or oro-pharyngeal swabs is the key clinical biomarker of COVID-19 and also the key clinical end point of pharmacological intervention.

Although antiviral, antibody, and immunomodulatory drugs are being used for treatment of various aspects of the infection, there are still few effective therapeutics for COVID-19 to date. To explore novel and effective therapeutic targets, we require a better understanding of the pathogenesis of COVID-19, particularly of virus–host interactions.[7] This will also enable more efficient disease management strategies, such as deriving prognostic information from viral load kinetics, and quantification of the effects of the immune system in controlling the disease. With limited studies on the *in vivo* dynamics of SARS-CoV-2, a mathematical modeling approach can be an excellent, complementary tool for investigating viral–host interactions and host immune response in order to better understand COVID-19 progression and evaluate treatment strategies. Indeed, the application of mathematical modeling and quantitative methods has been instrumental in our understanding of viral–host interactions of various viruses, including influenza, HIV, HBV, and HCV.[8] The kinetic models for the above viruses have been developed for various spatial scales, including molecular, cellular, multicellular, organ, and organism. By analyzing viral load kinetics, these models have deepened our understanding of the fundamentals of virus–host interaction dynamics, innate and acquired immune response, drug mechanisms of action, and drug resistance.[9−13]

While the fundamental principles governing different viral infections are similar among most viral species, the kinetics of the underlying mechanisms may vary based on the virus type. Researchers are already using mathematical models to understand the outbreak of COVID-19 in order to guide the efforts of governments worldwide in containing the spread of infection. While most of the models developed to date have focused on the epidemiological aspects of COVID-19 to understand the interhuman transmission dynamics of SARS-CoV-2,[14−18] there are a few studies that have investigated its virus–host interactions and pathogenesis. For example, Goyal et al. developed a mathematical model to predict the therapeutic outcomes of various COVID-19 treatment strategies.[19] Their model is based on target cell-limited viral dynamics[20] and incorporates the immune response to infection in order to predict viral load dynamics in patients pre- and post-treatment with various antiviral drugs. This model was used to project viral dynamics under hypothetical clinical scenarios involving drugs with varying potencies, different treatment timings postinfection, and levels of drug resistance, and the results of this study suggest the application of potent antiviral drugs prior to the peak viral load stage, i.e., in the presymptomatic stage, as an effective means of controlling infection in the body. Further, Wang et al. developed a prototype multiscale model to simulate SARS-CoV-2 dynamics at the tissue scale,[7] wherein an agent-based modeling approach was used to simulate intracellular viral replication and spread of infection to neighboring cells. To unravel the mechanistic underpinnings of clinical phenotypes of COVID-19, Sahoo et al. developed a mechanistic model that studies the intercellular

https://dx.doi.org/10.1021/acsptsci.0c00183
ACS Pharmacol. Transl. Sci. 2021, 4, 248−265

Table 1. List of Model Parameters Known A Priori

Notation	Definition	Units	Value (Hamster)	Value (Human)	ref
Immunity parameters					
D_{CD4}	Death rate of activated CD4 cells	d^{-1}		0.0185	68,69
D_P^S	Death rate of short-lived plasma cells	d^{-1}		0.5	70−72
D_P^L	Death rate of long-lived plasma cells	d^{-1}		0.0083	71,72
λ_{CD8}	Death rate of activated CD8 cells	d^{-1}		0.0139	73,69,68
D_{APC}	Death rate for activated APCs	d^{-1}		0.2	74−76
$\overline{APC}$	Generic steady state concentration of APCs	$cells{\cdot}mL^{-1}$		$10^{5.3}$	77
$\overline{APC}_L$	LRT steady state concentration of APCs	$cells{\cdot}mL^{-1}$		10^{6}	77,78
$\overline{APC}_M$	MPS steady state concentration of APCs	$cells{\cdot}mL^{-1}$		$10^{7.65}$	77,78
$\overline{CD8}$	Naïve CD8 steady state concentration	$cells{\cdot}mL^{-1}$		10^{5}	79
$\overline{BC}$	Naïve B cells steady state concentration	$cells{\cdot}mL^{-1}$		10^{5}	80,79
$\overline{CD4}$	Naïve CD4 steady state concentration	$cells{\cdot}mL^{-1}$		$10^{5.8}$	79
G_{APC}	Reequilibration rate of APCs	$cell{\cdot}mL{\cdot}d$		0.1	74,81
G_{CD8}	Reequilibration rate of naïve CD8 cells	$cell{\cdot}mL{\cdot}d$		0.0045	68,69
G_{BC}	Reequilibration rate of naïve B cells	$cell{\cdot}mL{\cdot}d$		1.75	82
G_{CD4}	Reequilibration rate of naïve CD4 cells	$cell{\cdot}mL{\cdot}d$		0.0027	69,68
G_{IFN}	Baseline IFN production rate	IFN units$\cdot mL^{-1}\cdot d^{-1}$	38.8	1.37	30,31
D_{IFN}	Degradation rate of IFN	d^{-1}	24	24	83
Healthy tissue parameters					
y_U^0	Initial concentration of target cells in URT	$cells{\cdot}mL^{-1}$	$10^{6.9}$	$10^{6.7}$	78,84,85
y_L^0	Initial concentration of target cells in LRT	$cells{\cdot}mL^{-1}$	$10^{6.9}$	$10^{6.7}$	84,85
y_G^0	Initial concentration of target cells in GI	$cells{\cdot}mL^{-1}$	$10^{7.4}$	$10^{6.9}$	86
y_M^0	Initial concentration of target cells in MPS	$cells{\cdot}mL^{-1}$	$10^{6.8}$	$10^{6.6}$	87−89
y_H^0	Initial concentration of target cells in heart	$cells{\cdot}mL^{-1}$	$10^{6.5}$	$10^{6.3}$	90,91
y_K^0	Initial concentration of target cells in kidneys	$cells{\cdot}mL^{-1}$	$10^{7.1}$	$10^{6.9}$	87,92
y_B^0	Initial concentration of target cells in brain	$cells{\cdot}mL^{-1}$	$10^{5.9}$	$10^{5.7}$	93,94
Viral dynamics parameters					
v_U^0	Initial concentration of viral load in URT	$virus{\cdot}mL^{-1}$	$10^{5.7}$	Table 3	30
Transport parameters					
Cl_{Ab}	Clearance rate of antibodies	d^{-1}		0.04	11
E	Hepatobiliary excretion rate	d^{-1}	2.68	0.15	95

interactions between infected cells and immune cells.[21] Also, Ke et al. developed a model to quantify the early dynamics of SARS-CoV-2 infection in the upper and lower respiratory tracts and used the model to predict infectiousness and disease severity based on viral load dynamics and immune response to infection.[22] Although also a target cell-limited model, by only including upper and lower respiratory tract compartments, this model omits key biological mechanisms involved in the complete immune response and is thus unable to provide deeper insights into the system-wide dynamics and interplay of disease response.

In order to improve upon the existing models, we have developed a multiscale semimechanistic model of viral dynamics, which, in addition to capturing virus-host interactions locally, is also capable of simulating the whole-body dynamics of SARS-CoV-2 infection and is thereby capable of providing insights into disease pathophysiology and the typical and atypical presentations of COVID-19. Importantly, using our modeling platform, we can identify treatment strategies for effective viral load suppression under various clinically relevant scenarios. We note that while the modeling platform is developed for SARS-CoV-2, we also expect it to be applicable to other viruses that have shared similarities in mechanisms of infection and physical dimensions.

RESULTS AND DISCUSSION

Model Development, Calibration, and Baseline Solution. We have developed a semimechanistic mathematical model to simulate the whole-body biodistribution kinetics of SARS-CoV-2 following infection through the nasal route (Figure 1; Methods: Model development). The model was formulated as a system of ordinary differential equations (eqs 1−40) that describe cellular-scale viral dynamics, whole-body transport and excretion of viruses, and innate and adaptive immune response to predict the viral load kinetics of SARS-CoV-2 in the respiratory tract, plasma, and other organs of the body. SARS-CoV-2 exhibits ACE2-tropism;[23] therefore, the organs included in the model were chosen based on the presence of ACE2 receptor expressing cells.[24−26] Specifically, the key processes described by the model include infection of ACE2-expressing susceptible cells by SARS-CoV-2 (also referred to as target cells), production of new virions by infected cells, death of infected cells due to cytopathic effects, transport of virions from the site of infection to other organs of the body, hepatobiliary excretion of the virions, and key processes in the innate and adaptive immune response against the virus and infected cells to clear the infection. Note that in the absence of a thorough understanding of the mechanistic underpinnings of viral shedding in the feces,[27] and a growing evidence of liver damage in COVID-19 patients,[28,29] we used bile production as the rate-limiting step for fecal excretion of the virus. Due to unavailability of *in vivo* or clinical data for viral excretion, it was not feasible to accurately estimate the excretion rate parameter; hence, we mechanistically modeled the process of fecal excretion by using the bile production rate as a surrogate for fecal excretion rate.

https://dx.doi.org/10.1021/acsptsci.0c00183
ACS Pharmacol. Transl. Sci. 2021, 4, 248−265

While some of the parameters of the model were known a priori (Table 1), the remaining parameters were estimated through nonlinear regression using published *in vivo*[30] and clinical[31] data. Specifically, from published experimental data for hamsters,[30] we first calibrated a reduced version of the model (referred to as Reduced model; eqs 1−23) that comprises all compartments and interferon (IFN)-mediated innate immunity but lacks adaptive immunity (bottom half of Figure 1; also see workflow in Figure 2). The parameters of the

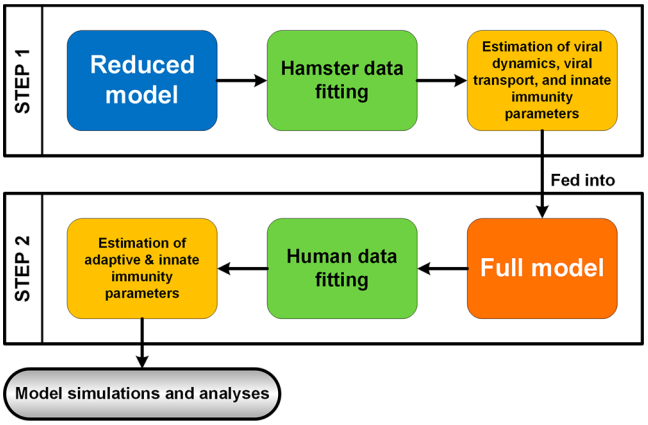

Figure 2. Modeling workflow. In the first step, the *reduced model* uses the hamster data to fit parameters corresponding to viral dynamics, transport coefficients, and innate immunity. Subsequently, the more complex *full model* uses the previously estimated parameters and clinical data to estimate the remaining parameters pertaining to the adaptive and innate immune responses. Lastly, simulations are generated to make predictions, and statistical analyses are performed to extract useful information.

reduced model characterize cellular-scale viral dynamics, IFN-mediated immunity, intercompartment viral transport, and hepatobiliary excretion of the virus from the mononuclear-phagocytic system (MPS). Note that in this model, the MPS compartment is the liver and spleen combined together. The estimated parameters were then used in the complete version of the model (referred to as Full model; eqs 1−40), which also includes adaptive immunity, to calibrate the remaining parameters using nonlinear regression with clinical data.[31] The models were solved numerically in MATLAB as an initial value problem, using the built-in stiff ODE solver *ode15s*.

Calibrating Parameters of the Reduced Model. As shown in Figure 3, the numerical solution of the reduced model for whole-body viral kinetics, IFN kinetics, and target cell population kinetics in hamsters satisfies the initial conditions and is in good agreement with the available *in vivo* data[30] for viral and IFN kinetics (Pearson correlation coefficient R between experimental data and model fits is >0.97, $p < 0.0001$, Figure S1a). The corresponding parameter estimates along with their 90% confidence intervals (CI) are given in Table 2. The Akaike information criterion (AIC) and Bayesian information criterion (BIC) values for the reduced model are 13.5 and 36.7, respectively. Based on findings in the *in vivo* study by Chan et al.[30] that the adaptive immune response in test animals was not triggered during the first 7 days postinfection, it is reasonable to use the reduced form of the model to estimate the unknown parameters, rather than using the full model at this point.

The model solution (Figure 3) shows the kinetics of ACE2-expressing target cells (solid orange lines) and their infected counterparts (dashed orange lines) in every compartment. These infected cells can produce new virions that will in turn infect other healthy target cells. Because we are using a target-cell limited modeling assumption,[10,19] the healthy target cells that become infected by the virus are not replaced by new healthy cells, and as shown in Figure 3, the target cells were observed to deplete within 48 h postinfection. The viral load kinetics (blue curve) is primarily governed by the interplay of new virion production, distribution of the virions between compartments, viral elimination by alveolar and MPS macrophages, hepatobiliary excretion of viruses from the body, cytopathic death of infected cells, and suppression of viral production due to IFN produced by infected cells,[10] which is shown in Figure 3i. As the infected cell population tapers, the IFN concentration will also decrease to the preinfection baseline value. In our model, infected respiratory tract cells are the source of IFN following infection, the lack of which has been found to be the underlying cause of life-threatening COVID-19 due to uncontrolled viral replication in the absence of IFN regulation.[32−34]

Of note, the plasma compartment (Figure 3h) of the model does not contain any target cell population and thus its viral load kinetics is only governed by the influx and outflux of viruses from various compartments. However, in the full model, the neutralization of viruses by antibodies will also be considered in the plasma compartment, as discussed in the next section. Plasma flow is the key mechanism of viral transport and systemic spread of infection in the body,[35] but due to lack of established mechanistic underpinnings of these processes, we instead use phenomenological rate constants to characterize viral transport. Based on the estimated characteristic times (1−24 h) of the vascular transport processes (shown in Figure 1 and presented as rates in Table 2), it can be inferred that viral transport is permeability-limited and not perfusion-limited, i.e., capillary permeability and vascular surface area govern the rate of extravasation of virions from blood vessels into tissue interstitium to reach the target cells, and thus viral transport is not exclusively governed by the plasma flow rates into the organs. This is consistent with the *in vivo* behavior of nanomaterials of comparable size[36−44] and is in contrast to the perfusion rate-limited kinetics of smaller lipophilic molecules. The variability in characteristic times of vascular transport can be explained by differences in the permeability of capillary endothelium due to differences in pore sizes of endothelial fenestrae.[45] For instance, the blood−brain barrier seems to resist transport of virus to the brain, thereby leading to an estimated characteristic influx time of 1 day, which is ∼20 times longer than the estimated characteristic time of influx to the MPS (1.25 h), which contains large sinusoidal pores in its microvasculature. Of note, the nonvascular transport processes have relatively longer characteristic times that can be attributed to resistance to transport offered by mucus or degradation caused by pH, among other factors.

Calibrating Parameters of the Full Model. Once the parameters discussed in the previous section were estimated, they were then used in the full model to calibrate the remaining parameters (see Table 3) relevant to the innate and adaptive immune system using published clinical data (n = 4 untreated patients with mild symptoms).[31] Due to the uncertainty associated with the duration between time of

https://dx.doi.org/10.1021/acsptsci.0c00183
ACS Pharmacol. Transl. Sci. 2021, 4, 248−265

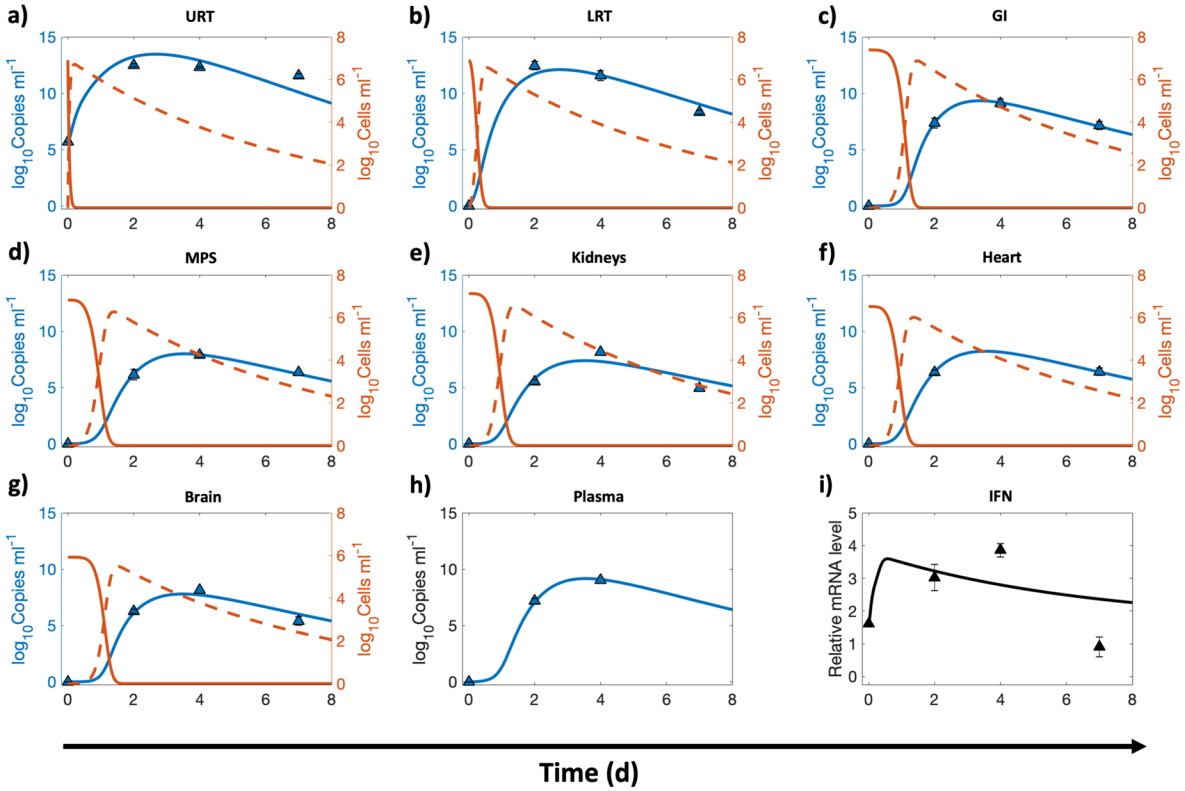

Figure 3. Whole-body reduced model calibration with *in vivo* data. Nonlinear least-squares regression of the whole-body reduced model using published *in vivo* data for hamsters is shown. The compartments under consideration are (a) upper respiratory tract (URT), (b) lower respiratory tract (LRT), (c) gastrointestinal tract (GI), (d) MPS, (e) kidneys, (f) heart, (g) brain, and (h) plasma. Orange solid and orange dashed lines indicate the population of healthy and infected ACE2-expressing target cells in a given compartment, respectively; the blue solid line represents the viral load in the corresponding compartment. The left *y*-axis represents viral load, and the right *y*-axis represents cell populations in (a) through (g). (i) Logarithm base 10 of IFN mRNA copies per γ-actin multiplied by 10^6 is shown. The triangular markers represent experimental data presented as mean ± SD (n = 5 animals per time point). Pearson correlation coefficient between observed and fitted values is $R > 0.97$ (Figure S1a).

infection and onset of symptoms (referred to as incubation period), a shifting parameter τ was included in the calibration routine. Numerically, the time points corresponding to the data were shifted τ units of time. As shown in Figure 4, the model correctly represents the initial conditions of the variables and predicts an incubation period τ of ∼6 days (indicated by the red arrow in Figure 4a), which is comparable to published literature.[46] Also, assuming the nasal route as the route of infection, the numerical solution for the upper respiratory tract (URT) at time $t = 0$ suggests exposure to a viral load of $\sim 10^7$ copies mL^{-1}. The clinical data shows the viral load kinetics in the upper (Figure 4a) and lower respiratory tract (Figure 4b), the IFN kinetics (Figure 4i), the effector $CD8^+$ (CD8*) and activated $CD4^+$ (CD4*) cell population kinetics (Figure 4k), and the total neutralizing antibody kinetics (Figure 4l). As shown in Figure 4, the full model solution fits the data well (Pearson correlation coefficient $R > 0.98$, $p < 0.0001$, Figure S1b) and predicts the kinetics of viral load in the remaining compartments by using the viral dynamics and transport parameters estimated from the *in vivo* data (through calibration of the reduced model). The AIC and BIC values for the full model are −3.04 and 24.5, respectively. The model predicts that the viral load in extrapulmonary organs and plasma persists for ∼17−20 days post onset of symptoms, consistent with published studies[47] and is thus comparable to the duration of viral detection in URT and lower respiratory tract (LRT), therefore suggesting that nasopharyngeal and oropharyngeal swabs can perhaps safely indicate the systemic level of viral load in the body. However, this modeling observation requires further experimental validation.

The model also shows the kinetics of naïve lymphocytes (Figure 4j) and antibody producing plasma cells (Figure 4k) in the lymphatic compartment, which is represented as a common compartment for the entire body. Importantly, in close agreement with published literature,[48,49] the model predicts that the systemic concentration of antibodies persists above the detectable limit for >100 days post onset of symptoms, following which it may no longer be detectable (Figure 4l). This finding suggests the lack of indefinite antibody protection against reinfection[50] and highlights the need for vaccine boosters to achieve long-lasting immunity.[51] We note that the data used in the above calibrations was obtained under conditions where neither the animals nor the patients were given any pharmacological treatment. Hence, the data are appropriate to calibrate the effects of the immune components and other physiological processes in distributing and eliminating the viral load.

While URT and LRT are the preferred sites to detect the presence of SARS-CoV-2, it is important to note, and as is evident from the model predictions, that the viral load in nonpulmonary organs can attain comparable levels and may thus explain the nonrespiratory symptoms observed in some COVID-19 patients.[29,52−56] Following transport of the virus from the respiratory tract to blood or via the gastrointestinal tract to blood, organs that have a significant population of

https://dx.doi.org/10.1021/acsptsci.0c00183
ACS Pharmacol. Transl. Sci. 2021, 4, 248−265

Table 2. List of Model Parameters Estimated from Fitting the Reduced Model to *In Vivo* Data[a]

Notation	Definition	Units	Value (90% CI)
Viral dynamics parameters			
I	Infection rate of target cells	mL·virus^{-1}·d^{-1}	4.05 (0–81.1)
P_v	Virus production rate in infected cells	virus·cell^{-1}·d^{-1}	19.03 (0–696)
D_1	Cytopathic death rate of infected cells	d^{-1}	0.15 (0–0.49)
Innate immunity parameters			
P_{IFN}	IFN production rate from infected cells	mRNA·mL·γ *actin*$^{-1}$ cell^{-1}·d^{-1}	3.67 (0–8.1)
ϵ	IFN efficacy	mRNA^{-1}·γ *actin*$^{-}$	2.59 (0–103)
$\lambda_L^{M\phi}$	Viral elimination rate by macrophages in LRT	d^{-1}	1.31 (0–9.3)
$\lambda_M^{M\phi}$	Viral elimination rate by macrophages in MPS	d^{-1}	4.24 (0–19.6)
Transport parameters			
C_1	URT to LRT viral transport rate	d^{-1}	0.73 (0.16–1.29)
C_2	URT to GI viral transport rate	d^{-1}	0.0016 (0–0.12)
A_1	Viral pulmonary absorption rate	d^{-1}	0.33 (0–8.6)
A_2	Viral intestinal absorption rate	d^{-1}	1.24 (0.16–2.3)
H_A	Hepatic artery-mediated viral transport rate	d^{-1}	19.2 (0–626)
H_V	Hepatic vein-mediated viral transport rate	d^{-1}	17.8 (0–715)
R_A	Renal artery-mediated viral transport rate	d^{-1}	8.5 (0–133)
R_V	Renal vein-mediated viral transport rate	d^{-1}	12.07 (0–165)
CO_A	Coronary artery-mediated viral transport rate	d^{-1}	7.2 (0–167)
CO_V	Coronary vein-mediated viral transport rate	d^{-1}	9.3 (0–186)
CA_A	Carotid artery-mediated viral transport rate	d^{-1}	0.97 (0–58.5)
J_V	Jugular vein-mediated viral transport rate	d^{-1}	2.32 (0–69.9)

[a]90% confidence intervals (CI) of the estimated parameters are shown in parentheses. For practical purposes, the negative value of the lower bounds of CIs has been replaced by zero. Note: Characteristic times corresponding to the transport parameters are shown in Figure 1.

Table 3. List of Model Parameters Estimated from Fitting the Full Model to Clinical Data[a]

Notation	Definition	Units	Value (90% CI)
Innate immunity parameters			
P_{IFN}	IFN production rate from infected cells	pg·cell^{-1}·d^{-1}	5.37 (0.7–10)
ϵ	IFN effectiveness	mL·pg^{-1}	4.57 (0.5–8.6)
Viral dynamics parameters			
v_U^0	Initial concentration of viral load in the URT	virus·mL^{-1}	$10^{6.9}$ ($10^{5.8}$ – $10^{7.9}$)
τ	Viral incubation time	d	5.77 (1.9–9.6)
Adaptive immunity parameters			
T_{APC}	Transition rate of naïve APCs into APC*	mL·virus^{-1}·d^{-1}	65.2 (0–1.3e+3)
$T_{T\text{-}cells}$	Transition rate of naïve CD8 into CD8* or CD4 into CD4*	mL·cell^{-1}·d^{-1}	0.0062 (0.005–0.007)
T_{BC}	Transition rate of naïve B cells into B*	mL·cell^{-1}·d^{-1}	0.029 (0–0.15)
T_{BC}^S	Transition rate of B* into short-lived plasma cells	mL·cell^{-1}·d^{-1}	564.8 (0–2.1e+4)
T_{BC}^L	Transition rate of B* into long-lived plasma cells	mL·cell^{-1}·d^{-1}	0.36 (0–16.5)
G_P^S	Production rate of antibodies from short-lived plasma cells	antibody·cell^{-1}·d^{-1}	0.59 (0–1.35)
G_P^L	Production rate of antibodies from long-lived plasma cells	antibody·cell^{-1}·d^{-1}	1.34 (0–90.2)
λ_{Ab}	Antibody loss rate due to viruses	mL·virus^{-1}·d^{-1}	0.0014 (0–0.004)
D_{Ab}	Elimination rate of viruses due to antibodies	mL·antibody^{-1}·d^{-1}	0.0085 (0–0.04)
D_{CD8}	Death rate of infected cells due to CD8*	mL·cell^{-1}·d^{-1}	0.0037 (0–0.01)

[a]90% confidence intervals (CI) of the estimated parameters are shown in parentheses. For practical purposes, the negative value of the lower bounds of CIs has been replaced by zero.

ACE2-expressing cells may become infected by the virus, leading to the extrapulmonary manifestations of COVID-19 that may include symptoms such as diarrhea and impaired renal-, hepatic-, cardiovascular-, or neurological-functions. This suggested relationship between organ viral load and extrapulmonary symptoms demands further experimental investigation and clinical validation.

Individualized Effects of Immune Components on Viral Kinetics. To investigate the effects of the cellular and humoral arms of innate and adaptive immunity on viral load kinetics in the body, we individually switched off these components and simulated the whole-body viral kinetics up to the time when viral load fell below the detectable limit[19] of 10^2 copies mL^{-1}. This numerical experiment is meant to mimic the effect of compromised immunity due to an underlying condition in a virtual patient undergoing no antiviral treatment. As seen in the viral kinetics shown in Figure 5, when one or all of the immune components were shut down, the viral concentration in all the compartments was higher than the baseline (dashed dark red line). Further, it can be inferred that IFN is the primary mechanism of controlling viral load in the URT (Figure 5a) and GI (Figure 5c), while macrophages (alveolar macrophages, Kupffer cells, and splenic macrophages) play a predominant role in limiting infection in the LRT, MPS, plasma, and other organs, followed by IFNs (Figures 5b, 5d–5h). Findings in the literature support the above observations as follows. Lack of IFNs can lead to excessive viral production[34] and cause life-threating COVID-19 in patients deficient in functional IFNs due to, for example, the occurrence of loss-of-function mutations in genes governing IFN-mediated immunity[33] or autoantibodies against IFNs.[32] Further, FABP4+ alveolar macrophages were observed to be largely absent in patients with severe COVID-19 but were the predominant macrophage in patients with mild disease,[57] indicating the major role of FABP4+ alveolar macrophages in controlling infection as also shown previously for patients with chronic obstructive pulmonary disease (COPD).[58] We assume a constant supply of macrophages in the lungs and MPS in our model, but a deleterious effect of infection on these immune cells cannot be ruled out, and further experimental evidence is necessary to model the macrophage population kinetics more appropriately.[59] Further, the model reveals that the effect of

https://dx.doi.org/10.1021/acsptsci.0c00183
ACS Pharmacol. Transl. Sci. 2021, 4, 248–265

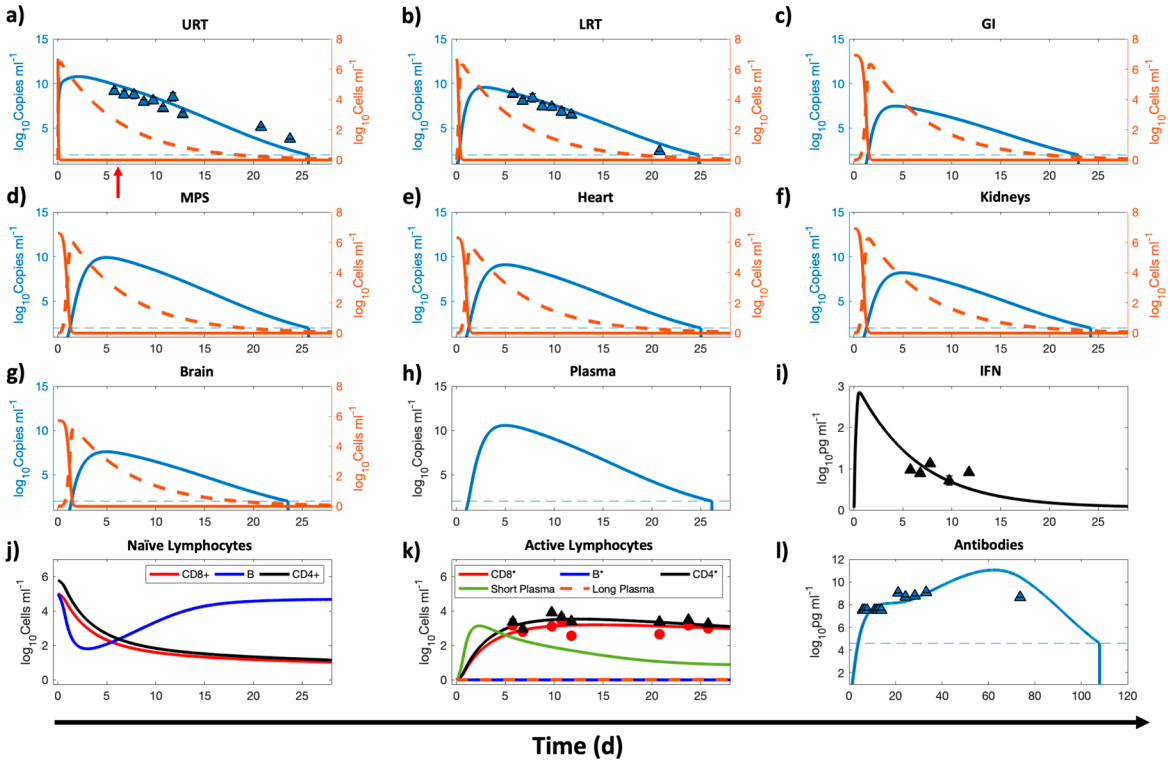

Figure 4. Whole-body full model calibration with clinical data. Numerical results for the full model, corresponding to the second step given in the modeling workflow in Figure 2 are shown. The compartments under consideration are (a) URT, (b) LRT, (c) GI, (d) MPS, (e) heart, (f) kidneys, (g) brain, (h) plasma, and (j, k, l) lymphatic compartment. Orange solid and orange dashed lines indicate the population of healthy and infected ACE2-expressing target cells in a given compartment, respectively, while the blue solid line represents the viral load in the corresponding compartment. The left *y*-axis represents viral load, and the right *y*-axis represents cell populations in panels (a) through (g). (i) Concentration kinetics of IFN. (j and k) Kinetics of adaptive immune system cells in the lymphatic compartment. (j) Naïve/immature $CD4^+$, $CD8^+$, and B cells. (k) Cells in their activated/effector state along with antibody producing plasma cells. (l) Concentration kinetics of total antibody (IgG, IgM, IgA). The red arrow in panel (a) indicates time of onset of symptoms. A lower bound at 10^2 copies mL^{-1} and $10^{4.6}$ pg mL^{-1} is imposed to represent the detectable limit of viral load and antibodies, respectively; the dashed blue line indicates the limit of detection. Once the viral load or antibodies go below the detection limit, a vertical line is used to indicate the time of occurrence of this event. The triangular markers represent clinical data presented as mean ± SD (n = 4 patients). The Pearson correlation coefficient between observed and fitted values is $R > 0.98$ (see Figure S1b).

adaptive immunity (antibodies and CD8* cells) is not significant in controlling infection, but it does not necessarily rule out the therapeutic potential of exogenously administered antibodies or novel cell-based therapies (e.g., T cell therapy).

All the above scenarios abstractly represent real-world underlying conditions (e.g., cancer, diabetes, autoimmune diseases) in patients that lead to varying degrees of immunosuppression, thus highlighting the importance of an individual's immune status in regulating SARS-CoV-2 kinetics. In the absence of immune responses, the only plausible mechanism that brings the viral load down is hepatobiliary excretion of the virus through the MPS, but our results show that it takes several weeks before the viral load falls below the detectable value of 10^2 copies mL^{-1}. Note that upon shutting down IFN- and macrophage-mediated immunity or total immunity, the viral load grew beyond clinically observed values in the literature ($\sim 10^{12}$ copies mL^{-1}); therefore, we set an upper bound at 10^{12} copies mL^{-1} to keep the results clinically meaningful.

Parametric Analysis. To identify the significance of model parameters in affecting viral load kinetics, we performed global sensitivity analysis using the full model (Figure 6). The model outputs used to investigate the influence of perturbations to input model parameters were area under the curves of viral load kinetics in URT, LRT, and plasma from 0 to 30 days (i.e., AUC_{0-30}^{URT}, AUC_{0-30}^{LRT}, and AUC_{0-30}^{Plasma}, respectively) and time to reduce the viral load to $<10^2$ copies mL^{-1} in URT, LRT, and plasma (i.e., t_{clear}^{URT}, t_{clear}^{LRT}, and t_{clear}^{Plasma}, respectively).

As shown in Figure 6a–f, multivariate linear regression analysis (MLRA)-based sensitivity indices provide insight into the relative importance of model parameters in governing viral load kinetics. The ranking obtained from MLRA (Figure 6g) suggests that the total viral load (AUC_{0-30}^{i}) in URT, LRT, and plasma (indicator of systemic behavior) is strongly dependent on viral production rate (P_v), IFN production rate (P_{IFN}), and cytopathic death rate of infected cells (D_1). Cytopathic death of infected cells is a property of the system that may be hard to manipulate pharmacologically; therefore, IFN concentration and viral production rate are conceivably the targets best-suited for pharmacological interventions to constrain the viral load in patients.[60] Treatment over a combination of the two parameters, i.e., IFN and viral production rates, can possibly be more efficient than monotherapy in suppressing viral load, but clinical validation of this hypothesis is necessary. While cytopathic death rate and viral production rate play major roles in governing the clearance time of viruses (t_{clear}^{i}), IFN production rate is relatively less significant. Further, transport processes play a significant role in governing both total viral load and time to clear the load. Specifically, the transport of virus from URT to LRT (C_1) affects viral load in URT and

https://dx.doi.org/10.1021/acsptsci.0c00183
ACS Pharmacol. Transl. Sci. 2021, 4, 248–265

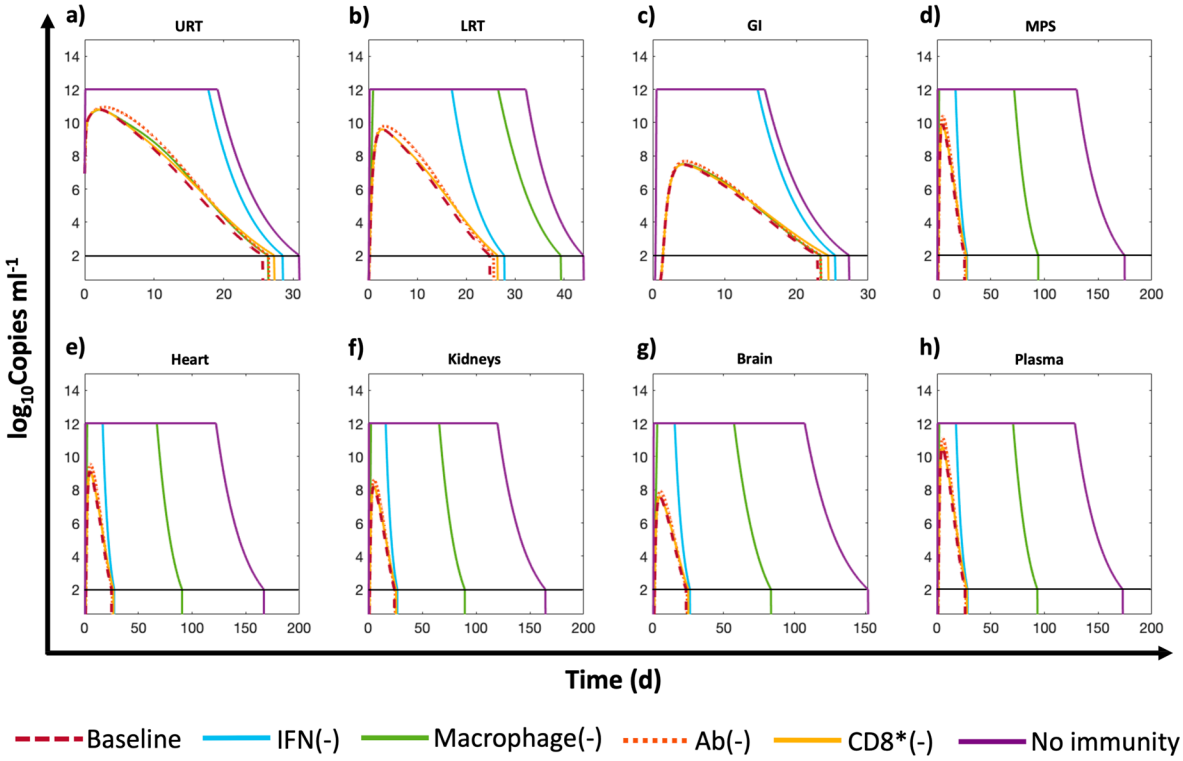

Figure 5. Effects of different components of the immune system. Comparison between different scenarios where a particular mechanism of immunity has been turned off is shown. The viral kinetics in a given compartment is presented on the *y*-axis. The compartments under consideration are (a) URT, (b) LRT, (c) GI, (d) MPS, (e) heart, (f) kidneys, (g) brain, and (h) plasma. Six scenarios are considered. (1) Baseline: All immune mechanisms are functional. (2) IFN(−): the innate immune effects of IFN are deactivated. (3) Macrophage(−): alveolar and MPS macrophages are eliminated. (4) Ab(−): no antibodies are produced. (5) CD8*(−): cytotoxic effects of CD8* are suppressed. (6) No immunity: all immunity mechanisms are absent. The flat line at 10^{12} copies mL^{-1} represents the upper bound imposed on viral load to showcase only clinically relevant results. A lower bound at 10^{2} copies mL^{-1} is imposed to represent the detectable limit of viral load in the body, indicated by the horizontal black line; once the viral load goes below the detection limit, a vertical line is used to indicate the time of occurrence of this event.

viral transport from blood to MPS via the hepatic artery (H_A) and MPS to blood via the hepatic vein (H_V) govern the clearance time from plasma, which should also affect the viral clearance of other organs connected to plasma. Also, the elimination rates of viruses by alveolar macrophages ($\lambda_L^{M\phi}$) and MPS macrophages ($\lambda_M^{M\phi}$) are important parameters in governing the kinetics of viral load in LRT and plasma, respectively. Finally, the total viral load in LRT is also affected by pulmonary absorption (A_1), i.e., by the rate of transport of viruses from LRT to plasma.

Clinical Application of Model. Up to this point, we calibrated the reduced model with *in vivo* data and used the estimated parameters to calibrate the remaining parameters of the full model with clinical data for patients with mild symptoms. While the full model was able to produce observations consistent with published literature, the validation of viral load kinetics of the extrapulmonary organs needs corroboration from future clinical studies. However, to demonstrate the possible clinical utility of our model, we next sought to examine whether this tool can make predictions that might allow clinicians to design an effective therapy for patients, helping to optimize and personalize their treatment regimen. As a numerical experiment, we tested three treatment scenarios in controlling infection: a hypothetical antiviral agent, interferon therapy, and antiviral agent−interferon combination therapy. Further, the effects of the timing of therapy initiation (t^T) were also tested, i.e., starting therapy on the day of onset of symptoms ($t^T = t^{onset}$) and starting therapy 5 days post onset of symptoms ($t^T = t^{onset} + 5$). To quantify treatment effectiveness, we compared the viral load kinetics in three compartments, namely, URT, LRT, and plasma in simulations spanning a period of 4 weeks.

Antiviral Therapy. We simulated therapy with a *hypothetical antiviral agent that has the same mechanism of action as Remdesivir*,[61] i.e. interference with RNA-dependent RNA polymerase. For this, 200 mg loading dose (≡initial plasma concentration $C_0 = 5\ \mu M$, assuming a molecular weight of 800 g/mol and a volume of distribution of 50 L), followed by 100 mg daily maintenance doses for 9 additional days via intravenous injection were simulated to mimic the pharmacological intervention. Treatment was started at one of the two time points previously mentioned. As a simplification, assuming one-compartment pharmacokinetics for the hypothetical drug with elimination rate constant $k_{Cl} = 1\ d^{-1}$, we use the plasma concentration kinetics as a surrogate for tissue concentration kinetics of the drug. The plasma concentration $\alpha_V(t)$ is thus given by

$$\alpha_V(t) = \sum_{i \text{ in } S^T} C_0 \cdot 1_{t \geq i}(t) \exp(-k_{Cl} \cdot (t - i))$$

where $1_{t \geq i}(t) = \begin{cases} 1, & t \geq i \\ 0, & t < i \end{cases}$.

Hence, the injection times are $i = t^T, t^T + 1, \ldots, t^T + 9$, and we define this set of times as S^T. The antiviral agent acts by inhibiting the production rate P_v of virus from infected cells in the body, such that $P_v(t)$ is scaled by $\frac{1}{1 + EC_{50}^{-1} \cdot \alpha_V(t)}$, where EC_{50}

https://dx.doi.org/10.1021/acsptsci.0c00183
ACS Pharmacol. Transl. Sci. 2021, 4, 248−265

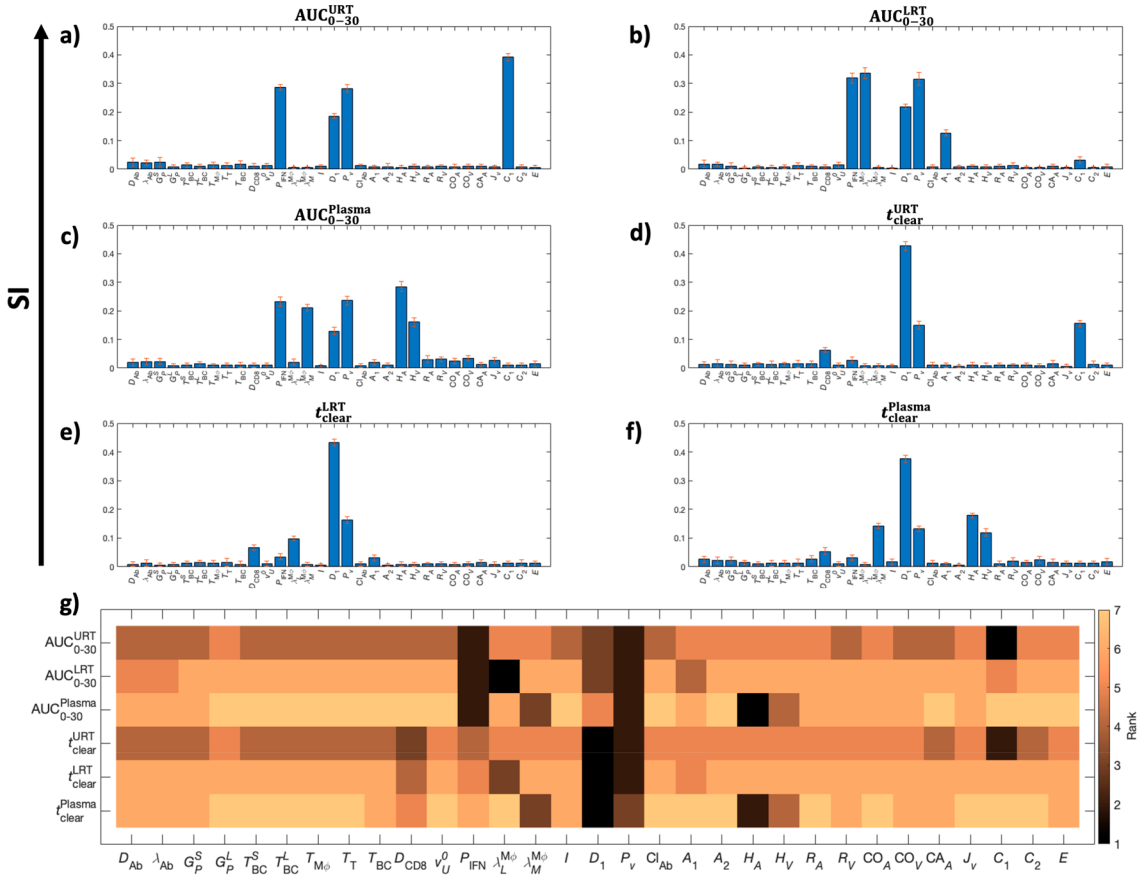

Figure 6. Global sensitivity analysis. All parameters are perturbed simultaneously from their reference value. (a–f) The ranking of each parameter is quantified as the sensitivity index (SI, *y*-axis) measured under six criteria. The first three are area under the curves of viral load kinetics (AUC^{i}_{0-30}) for the first 30 days in the (a) URT, (b) LRT, and (c) plasma compartment. The next three are the total time (t^{i}_{clear}) required for the viral load to fall below the detectable concentration of 10^2 copies mL^{-1} in the (d) URT, (e) LRT, and (f) plasma compartment. Each SI is accompanied by an error bar resulting from the sampling distribution. (g) Heat map indicating the ranking of the parameters based on the magnitude of the sensitivity index.

is the half maximal effective concentration of the drug, chosen to be 0.77 μM. Plasma concentration kinetics $\alpha_V(t)$ of the drug are shown in the inset of Figure 7a for the scenario when the treatment was initiated on the day of onset of symptoms.

As shown in Figure 7a–c, under the considered therapeutic regimen, the antiviral therapy shows a significant impact on viral load reduction compared to the no treatment scenario, irrespective of the timing of therapy initiation. However, early initiation of antiviral therapy led to a lesser total viral load and a faster reduction of the load, which is consistent with results of other studies.[19]

Interferon Therapy. We simulated treatment with interferon beta-1a, with and without the hypothetical antiviral agent (discussed above). For this, four subcutaneous injections (Dose = 44 μg each) of interferon beta-1a were administered every other day starting at one of the two time points previously mentioned. The plasma concentration kinetics of interferon beta-1a $\alpha_I(t)$ is obtained by solving the following equation:

$$\frac{d\alpha_I(t)}{dt} = \sum_{i \text{ in } Q^T} k_{absorp} \frac{Dose}{V_{sc}} 1_{t \geq i}(t) \exp(-k_{absorp}(t - i)) - k_{excr}\alpha_I(t)$$

where $1_{t \geq i}(t) = \begin{cases} 1, & t \geq i \\ 0, & t < i \end{cases}$.

Hence, the injection times are $i = t^T, t^T + 2, t^T + 4, t^T + 6$, and we define this set of times as Q^T. The plasma concentration kinetics $\alpha_I(t)$ of interferon beta-1a is shown in the inset of Figure 7d for the scenario when the treatment was initiated on the day of onset of symptoms. Here, the parameters k_{absorp}, V_{sc}, and k_{excr}, which represent the absorption of interferon beta-1a from the site of injection to the bloodstream, volume of the injection site, and excretion rate of interferon beta-1a, respectively, were estimated by fitting the above equation to literature derived concentration kinetics data.[62] The estimated parameter values are: k_{absorp} = 7.04 d^{-1},V_{sc} = 3.43 mL, and k_{excr} = 0.074 d^{-1}. Of note, while interferon beta-1a acts in the same way as endogenous IFN, i.e. by inhibiting the production rate P_v of virus from infected cells, we model them separately to accommodate the possibility of unique pharmacokinetic properties of the two agents. Therefore, the first term of viral load kinetics in the ODE for organ *i* (see Methods) now becomes $P_v \frac{y_i^I(t)}{1 + \varepsilon(IFN(t) + \alpha_I(t))}$.

As shown in Figure 7d–f, interferon beta-1a therapy significantly reduces the viral load, and the effect is comparable to the hypothetical antiviral agent. Also, early initiation of therapy leads to a lesser total viral load and a faster reduction in viral load.

Combination Therapy. Finally, we tested the effect of the combination of the hypothetical antiviral agent and interferon

https://dx.doi.org/10.1021/acsptsci.0c00183
ACS Pharmacol. Transl. Sci. 2021, 4, 248–265

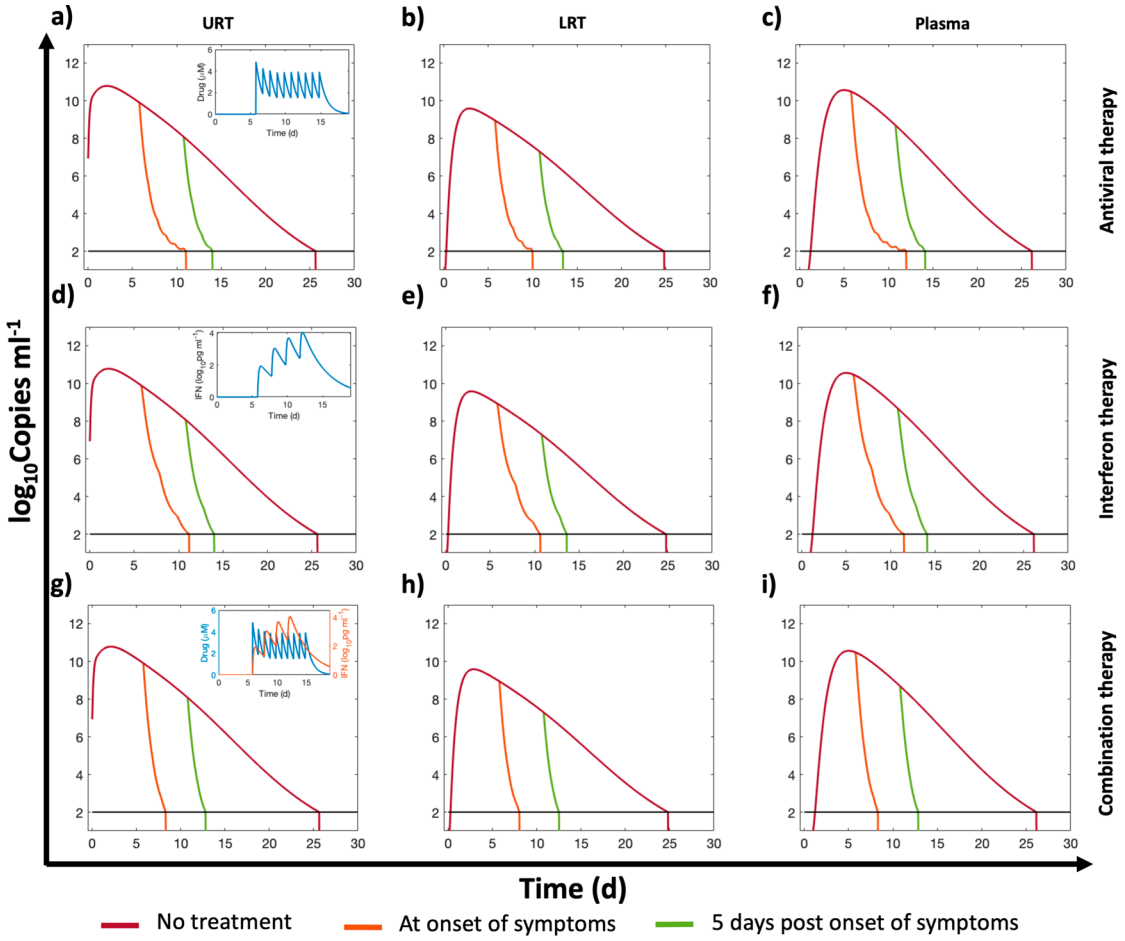

Figure 7. Simulated pharmacological interventions. Viral load kinetics in URT, LRT, and plasma following (a–c) treatment with a hypothetical antiviral agent, (d–f) treatment with interferon beta-1a, (g–i) and combination of the antiviral and interferon beta-1a, starting on the day of onset of symptoms (orange line) and 5 days post onset of symptoms (green), compared against no treatment (burgundy). Insets in panels a, d, and g show plasma concentration kinetics of the pharmacological agent/s for the treatment regimen that begins on the day of onset of symptoms. A lower bound at 10^2 copies mL^{-1} is imposed to represent the detectable limit of viral load in the body (black horizontal line); once the viral load goes below the detection limit, a vertical line is used to indicate the time of occurrence of this event.

beta-1a on viral load kinetics (plasma concentration kinetics in the inset of Figure 7g). As shown in Figure 7g–i, the combination therapy leads to a faster reduction in viral load compared to the effect of antiviral agent or interferon beta-1a alone, such that the viral load seems to fall below the detection threshold 2–3 days earlier. However, the need for clinical validation of this model prediction must be emphasized.

CONCLUSION

In summary, we have developed a semimechanistic (i.e., partially mechanistic and partially phenomenological) mathematical model that predicts the whole-body viral distribution kinetics of SARS-CoV-2 by incorporating cellular-scale viral dynamics, relevant physiological processes of viral transport, innate and adaptive immune response, and viral excretion. The model is well calibrated with published *in vivo* and clinical data and provides insights into the importance of various components of the immune system in controlling infection. Through global sensitivity analysis, we identified the key mechanisms that control infection and can be used as potential therapeutic targets for pharmacological intervention. Finally, we tested the potential of such therapeutic targets by simulating clinically relevant treatment options and identified the importance of the timing of treatment initiation and the effects of various therapies that may effectively suppress infection. As a limitation of the model, it is important to note that due to lack of clinical data for the viral load kinetics in extrapulmonary compartments, we had to rely on the transport parameters estimated from *in vivo* data, and the model predictions for the extrapulmonary compartments could not be clinically validated. Also, due to limited availability of data for cytokines in the hamster and clinical studies, the IFN-mediated inhibitory effects on viral production were calibrated with data for interferon-γ only. As clinical knowledge of the disease and its mechanisms improves, we will continue to fine-tune the model and integrate it with a physiologically based pharmacokinetic model to build an in-silico platform that can be used to simulate disease progression and a more complete pharmacokinetics of various test drugs and novel formulations.

METHODS

Model Development. In each organ compartment, we consider the kinetics of three populations. The first is the concentration of healthy cells, denoted by $y_i^H(t)$, where i is an arbitrary compartment. The second is the concentration of infected cells, denoted by $y_i^I(t)$, and the third is the concentration of viral particles $v_i(t)$. The compartments that we consider are $i = [U, L, G, M, H, K, B]$, where U is the upper

https://dx.doi.org/10.1021/acsptsci.0c00183
ACS Pharmacol. Transl. Sci. 2021, 4, 248–265

respiratory tract (URT), L is the lower respiratory tract (LRT), G is the gastrointestinal tract (GI), M is the mononuclear phagocytic system (MPS), which encompasses the liver and the spleen, H is the heart, K denotes the kidneys, and B is the brain. All organ compartments are connected via the plasma compartment $P(t)$, in which we only consider the concentration of viral particles in systemic circulation.

We assume that, due to the time scale under consideration, the population of healthy cells does not replenish during the simulation window. Thus, the rate of change of healthy cells is modeled as a decreasing function, which depends on the interaction between healthy cells and the surrounding viral particles that infect them. The conversion rate of healthy cells to infected cells is denoted by the infection rate I.

The rate of change of total infected cell population within an organ is a function of three mechanisms. The first is an increase due to freshly infected healthy cells by viral particles, the second is death due to the cytopathic effects of viral infection, proportional to the number of infected cells and characterized by the rate constant D_1, and the third is due to the interaction between effector $CD8^+$ cells (concentration denoted by $CD8^*(t)$) and the infected cells. The cytotoxic effect is measured in terms of the death rate constant D_{CD8}. It is important to note that in the reduced form of the model, infected cell death due to effector CD8* cells is not included. In our model description, all activated immune cells are indicated with an asterisk (e.g., CD8*), while inactive or naïve populations are indicated by standard naming conventions (e.g., $CD8^+$).

The concentration of viral particles in each organ compartment is influenced by different factors, some of which are organ-specific. However, in all organ compartments, the rate of change of viral particles is proportional to the number of infected cells with virus production constant P_v but is inversely proportional to the concentration of IFN, denoted IFN(t). IFN is part of the innate immune response that acts by suppressing the viral production rate of infected cells and is controlled by the effectiveness constant ε. In all compartments, viral particles may be neutralized due to the aggregation of antibodies on their surface proteins. The antibody concentration is represented by Ab(t), and the destruction rate of viral particles due to antibodies is denoted by D_{Ab}. Of note, neutralization of virus by antibodies is not incorporated in the reduced form of the model. Lastly, the viral load can also be reduced by tissue resident macrophages in the lungs (alveolar macrophages) and MPS (Kupffer cells and splenic macrophages) that engulf the viral particles and destroy them. The rate of removal of viral particles by macrophages is given by $\lambda_i^{M\phi}$.

We introduce the system of ordinary differential equations that governs the concentration kinetics as follows. Mechanisms particular to each compartment are discussed after each set of equations.

Equations for the URT:

$$\frac{d}{dt}y_U^H(t) = -Iy_U^H(t)\, v_U(t), \qquad y_U^H(0) = y_U^0 \tag{1}$$

$$\frac{d}{dt}y_U^I(t) = Iy_U^H(t)\, v_U(t) - D_1 y_U^I(t) - D_{CD8} y_U^I(t)\, CD8^*(t), \qquad y_U^I(0) = 0 \tag{2}$$

$$\frac{d}{dt}v_U(t) = P_v \frac{y_U^I(t)}{1+\varepsilon \mathrm{IFN}(t)} - C_1 v_U(t) - C_2 v_U(t) - D_{Ab} v_U(t)\, \mathrm{Ab}(t), \qquad v_U(0) = v_U^0 \tag{3}$$

Note that the rate of change of viral particles in the URT depends on two clearance mechanisms. These consist of the migration of viral particles from the URT to the LRT and from the URT to the GI tract. The corresponding transport coefficients are C_1 and C_2, respectively.

Equations for the LRT:

$$\frac{d}{dt}y_L^H(t) = -Iy_L^H(t)\, v_L(t), \qquad y_L^H(0) = y_L^0 \tag{4}$$

$$\frac{d}{dt}y_L^I(t) = Iy_L^H(t)\, v_L(t) - D_1 y_L^I(t) - D_{CD8} y_L^I(t)\, CD8^*(t), \qquad y_L^I(0) = 0 \tag{5}$$

$$\frac{d}{dt}v_L(t) = P_v \frac{y_L^I(t)}{1+\varepsilon \mathrm{IFN}(t)} + C_1 v_L(t) - A_1 v_L(t) - D_{Ab} v_L(t)\, \mathrm{Ab}(t) - \lambda_L^{M\phi} v_L(t), \qquad v_L(0) = 0 \tag{6}$$

Viral particles in the LRT are received from the URT but are also lost to the systemic circulation, which is quantified through the pulmonary absorption coefficient A_1.

Equation for IFN:

$$\frac{d}{dt}\mathrm{IFN}(t) = G_{IFN} + P_{IFN}(y_U^I(t) + y_L^I(t)) - D_{IFN}\mathrm{IFN}(t), \qquad \mathrm{IFN}(0) = \mathrm{IFN}_0 \tag{7}$$

As mentioned earlier, IFN limits the production of viral particles by infected cells. The rate of production of this cytokine is regulated by two effects. One is a zeroth order generation term G_{IFN}, and the second is proportional to the cumulative population of infected cells in the respiratory tract. The proportionality constant in the second mechanism is P_{IFN}. Further, IFN can degrade over time at a rate given by D_{IFN}.

Equations for the GI tract:

$$\frac{d}{dt}y_G^H(t) = -Iy_G^H(t)\, v_G(t), \qquad y_G^H(0) = y_G^0 \tag{8}$$

$$\frac{d}{dt}y_G^I(t) = Iy_G^H(t)\, v_G(t) - D_1 y_G^I(t) - D_{CD8} y_G^I(t)\, CD8^*(t), \qquad y_G^I(0) = 0 \tag{9}$$

$$\frac{d}{dt}v_G(t) = P_v \frac{y_G^I(t)}{1+\varepsilon \mathrm{IFN}(t)} + C_2 v_U(t) - A_2 v_G(t) - D_{Ab} v_G(t)\, \mathrm{Ab}(t), \qquad v_G(0) = 0 \tag{10}$$

Within the GI tract, in addition to the standard mechanisms, viral particles can be lost to the liver via the hepatic portal vein. This rate is quantified through the intestinal absorption rate A_2. Additionally, as discussed above, viral particles from the URT are transported to the GI tract at a rate C_2.

Equations for the MPS:

$$\frac{d}{dt}y_M^H(t) = -Iy_M^H(t)\, v_M(t), \qquad y_M^H(0) = y_M^0 \tag{11}$$

https://dx.doi.org/10.1021/acsptsci.0c00183
ACS Pharmacol. Transl. Sci. 2021, 4, 248−265

$$\frac{d}{dt}y_M^I(t) = Iy_M^H(t)\, v_M(t) - D_1 y_M^I(t) - D_{CD8} y_M^I(t)\ \mathrm{CD8}^*(t), \qquad y_M^I(0) = 0 \tag{12}$$

$$\frac{d}{dt}v_M(t) = P_v \frac{y_M^I(t)}{1 + \varepsilon \mathrm{IFN}(t)} + A_2 v_G(t) + H_A P(t) - H_V v_M(t) - E v_M(t) - D_{Ab} v_M(t)\ \mathrm{Ab}(t) - \lambda_M^{M\phi} v_M(t), \qquad v_M(0) = 0 \tag{13}$$

The rate of change of viral particles within the MPS can increase due to the particles collected from the GI tract (A_2) and those incoming from systemic circulation through the hepatic artery (H_A). At the same time, particles can leave this compartment through the hepatic vein (H_V) or through the hepatobiliary excretion mechanism (E).

Equations for the heart:

$$\frac{d}{dt}y_H^H(t) = -Iy_H^H(t)\, v_H(t), \qquad y_H^H(0) = y_H^0 \tag{14}$$

$$\frac{d}{dt}y_H^I(t) = Iy_H^H(t)\, v_H(t) - D_1 y_H^I(t) - D_{CD8} y_H^I(t)\ \mathrm{CD8}^*(t), \qquad y_H^I(t) = 0 \tag{15}$$

$$\frac{d}{dt}v_H(t) = P_v \frac{y_H^I(t)}{1 + \varepsilon \mathrm{IFN}(t)} + \mathrm{CO}_A P(t) - \mathrm{CO}_V v_H(t) - D_{Ab} v_H(t)\ \mathrm{Ab}(t), \qquad v_H(t) = 0 \tag{16}$$

Similar to the MPS, the rate of change of viral particles in the heart depend on two fluxes. One is the incoming viral load from systemic circulation through the coronary arteries (CO_A), and the second is the outgoing viral particles via the coronary veins (CO_V).

Equations for the kidneys:

$$\frac{d}{dt}y_K^H(t) = -Iy_K^H(t)\, v_K(t), \qquad y_K^H(t) = y_K^0 \tag{17}$$

$$\frac{d}{dt}y_K^I(t) = Iy_K^H(t)\, v_K(t) - D_1 y_K^I(t) - D_{CD8} y_K^I(t)\ \mathrm{CD8}^*(t), \qquad y_K^I(t) = 0 \tag{18}$$

$$\frac{d}{dt}v_K(t) = P_v \frac{y_K^I(t)}{1 + \varepsilon \mathrm{IFN}(t)} + R_A P(t) - R_V v_K(t) - D_{Ab} v_K(t)\ \mathrm{Ab}(t), \qquad v_K(t) = 0 \tag{19}$$

Given that the size of the SARS-CoV-2 virus is ∼100 nm, we assume that renal excretion is not feasible.[63] Therefore, the viral kinetics in kidneys is dependent on the standard mechanisms of influx via the renal arteries (R_A) and outflux via the renal veins (R_V).

Equations for the brain:

$$\frac{d}{dt}y_B^H(t) = -Iy_B^H(t)\, v_B(t), \qquad y_B^H(t) = y_B^0 \tag{20}$$

$$\frac{d}{dt}y_B^I(t) = Iy_B^H(t)\, v_B(t) - D_1 y_B^I(t) - D_{CD8} y_B^I(t)\ \mathrm{CD8}^*(t), \qquad y_B^I(t) = 0 \tag{21}$$

$$\frac{d}{dt}v_B(t) = P_v \frac{y_B^I(t)}{1 + \varepsilon \mathrm{IFN}(t)} + \mathrm{CA}_A P(t) - J_V v_B(t) - D_{Ab} v_B(t)\ \mathrm{Ab}(t), \qquad v_B(t) = 0 \tag{22}$$

While the blood−brain barrier may be deterrent to the establishment of infection in the brain, we have included the brain compartment due to the lack of evidence for the former.[64] Analogous to the heart and kidney compartments, the brain receives viral particles delivered through systemic circulation via the internal carotid arteries (CA_A). Subsequently, viral particles can rejoin the plasma compartment by means of the internal jugular veins (J_V).

Equations for plasma:

$$\frac{d}{dt}P(t) = A_1 v_L(t) + H_V v_M(t) + R_V v_K(t) + \mathrm{CO}_V v_H(t) + J_V v_B(t) - H_A P(t) - R_A P(t) - \mathrm{CO}_A P(t) - \mathrm{CA}_A P(t) - D_{Ab} P(t)\ \mathrm{Ab}(t), \qquad P(t) = 0 \tag{23}$$

The equation for the plasma compartment incorporates all the outgoing fluxes of viral particles through arteries (H_A, R_A, CO_A, CA_A) and the incoming fluxes via veins (H_V, R_V, CO_V, j_V). Also, the viral load from LRT in eq 6 gets added to plasma at rate A_1. Lastly, similar to all the previous compartments, viral particles can be neutralized by antibodies at a rate D_{Ab} (in the *full model* only).

The model up to this point is the **reduced model**, and the only equation that captures the immune system is eq 7. This equation describes the change of concentration of IFN, which is part of the innate immune system. However, the adaptive immune system should activate to properly mount a full immune response. The equations that follow provide the remaining elements to initiate and maintain a humoral and cell-mediated adaptive immune response to make up the **full model**.

Equations 24−30 model the concentration of naïve antigen presenting cells (APCs) $\mathrm{APC}_i(t)$ in a given compartment i. These cells predominantly act as carriers, transporting remnants of viral particles to the lymphatic compartment to raise the alarm in the adaptive arm of the immune system. In order to keep the population of APCs at steady state, a replenishing mechanism is included. It is proportional to the difference between the current concentration $\mathrm{APC}_i(t)$, and the generic steady state value $\overline{\mathrm{APC}}$, divided by the absolute value of the same difference plus a modulating constant that we set = 1, i.e., $\frac{(\mathrm{APC}_i(t) - \overline{\mathrm{APC}})}{1 + |\mathrm{APC}_i(t) - \overline{\mathrm{APC}}|}$. The rationale behind the previous definition is that if the concentration $\mathrm{APC}_i(t)$ is close to $\overline{\mathrm{APC}}$, the term is essentially zero, whereas if the difference is large, the denominator is equally large, and the ratio is close to one. This allows a near constant modulation rate that only acts whenever the population of macrophages is far from equilibrium. This reequilibration rate is denoted by G_{APC}. The APC population is also impacted by the interaction between APCs and invading viral particles. This causes the population of APCs to become activated at a rate T_{APC}, which is proportional to the product of the concentration of these cells and the viral load.

Equations for URT naïve APCs:

https://dx.doi.org/10.1021/acsptsci.0c00183
ACS Pharmacol. Transl. Sci. 2021, 4, 248−265

$$\frac{d}{dt}\mathrm{APC}_U(t) = -G_{\mathrm{APC}}\frac{(\mathrm{APC}_U(t) - \overline{\mathrm{APC}})}{1 + |\mathrm{APC}_U(t) - \overline{\mathrm{APC}}|} - T_{\mathrm{APC}}\mathrm{APC}_U(t)\, v_U(t),$$
$$\mathrm{APC}_U(t) = \overline{\mathrm{APC}} \tag{24}$$

Equations for the LRT naïve APCs:

$$\frac{d}{dt}\mathrm{APC}_L(t) = -G_{\mathrm{APC}}\frac{(\mathrm{APC}_L(t) - \overline{\mathrm{APC}}_L)}{1 + |\mathrm{APC}_L(t) - \overline{\mathrm{APC}}_L|} - T_{\mathrm{APC}}\mathrm{APC}_L(t)\, v_L(t),$$
$$\mathrm{APC}_L(t) = \overline{\mathrm{APC}}_L \tag{25}$$

GI tract naïve APCs:

$$\frac{d}{dt}\mathrm{APC}_G(t) = -G_{\mathrm{APC}}\frac{(\mathrm{APC}_G(t) - \overline{\mathrm{APC}})}{1 + |\mathrm{APC}_G(t) - \overline{\mathrm{APC}}|} - T_{\mathrm{APC}}\mathrm{APC}_G(t)\, v_G(t),$$
$$\mathrm{APC}_G(t) = \overline{\mathrm{APC}} \tag{26}$$

MPS naïve APCs:

$$\frac{d}{dt}\mathrm{APC}_M(t) = -G_{\mathrm{APC}}\frac{(\mathrm{APC}_M(t) - \overline{\mathrm{APC}}_M)}{1 + |\mathrm{APC}_M(t) - \overline{\mathrm{APC}}_M|} - T_{\mathrm{APC}}\mathrm{APC}_M(t)\, v_M(t),$$
$$\mathrm{APC}_M(t) = \overline{\mathrm{APC}}_M \tag{27}$$

Heart naïve APCs:

$$\frac{d}{dt}\mathrm{APC}_H(t) = -G_{\mathrm{APC}}\frac{(\mathrm{APC}_H(t) - \overline{\mathrm{APC}})}{1 + |\mathrm{APC}_H(t) - \overline{\mathrm{APC}}|} - T_{\mathrm{APC}}\mathrm{APC}_H(t)\, v_H(t),$$
$$\mathrm{APC}_H(t) = \overline{\mathrm{APC}} \tag{28}$$

Kidney naïve APCs:

$$\frac{d}{dt}\mathrm{APC}_K(t) = -G_{\mathrm{APC}}\frac{(\mathrm{APC}_K(t) - \overline{\mathrm{APC}})}{1 + |\mathrm{APC}_K(t) - \overline{\mathrm{APC}}|} - T_{\mathrm{APC}}\mathrm{APC}_K(t)\, v_K(t),$$
$$\mathrm{APC}_K(t) = \overline{\mathrm{APC}} \tag{29}$$

Brain naïve APCs:

$$\frac{d}{dt}\mathrm{APC}_B(t) = -G_{\mathrm{APC}}\frac{(\mathrm{APC}_B(t) - \overline{\mathrm{APC}})}{1 + |\mathrm{APC}_B(t) - \overline{\mathrm{APC}}|} - T_{\mathrm{APC}}\mathrm{APC}_B(t)\, v_B(t),$$
$$\mathrm{APC}_B(t) = \overline{\mathrm{APC}} \tag{30}$$

Lymphatic activated APCs:

$$\frac{d}{dt}\mathrm{APC}^*(t) = T_{\mathrm{APC}}\left(\sum_{i \text{ in } \{U,L,G,M,H,K,B\}} \mathrm{APC}_i(t)\, v_i(t)\right) - D_{\mathrm{APC}}\mathrm{APC}^*(t),$$
$$\mathrm{APC}^*(t) = 0 \tag{31}$$

As mentioned earlier, the concentration of activated APCs, denoted by $\mathrm{APC}^*(t)$, increases at a rate proportional to the conversion rate T_{APC} of naïve APCs to the activated state. At the same time, activated APCs can become incapacitated or simply eliminated after a certain period of time. These processes are pooled into the APC death rate constant D_{APC}.

The remaining equations in the model describe either lymphocyte or antibody concentrations. The lymphocytes under consideration are $\mathrm{CD8}^+$, $\mathrm{CD4}^+$, and B cells. The concentration of the naïve or inactivated version of these populations is represented by $\mathrm{CD8}(t)$, $\mathrm{CD4}(t)$, and $\mathrm{BC}(t)$, respectively. Similar to the APC case, the steady state concentration for each of these cell types is denoted with a horizontal bar on top of each variable. This value is maintained using a mechanism analogous to the APC case, i.e., through the term $-G_X\frac{(X(t) - \bar{X})}{1 + |X(t) - \bar{X}|}$, where X is the corresponding cell type.

Furthermore, each of these lymphocytes can be promoted to its activated state, which we denote with an asterisk, X^*. This conversion takes place when activated APCs interact with naïve lymphocytes, presenting them fragments of the ingested viral particles. The transformation rate from the naïve state to the activated one is represented by the constant T_X, where X indicates the cell type. For the case of $\mathrm{CD4}^+$ and $\mathrm{CD8}^+$, we use the common rate T_{T}. The concentration of activated lymphocytes can fluctuate due to two mechanisms. One is the conversion of naïve cells, which was already discussed. The second is due to death caused by a variety of factors, such as exhaustion or apoptosis, and is expressed through the death constant D_X. B cells, however, follow a different mechanism, which we discuss later.

Naïve CD8:

$$\frac{d}{dt}\mathrm{CD8}(t) = -G_{\mathrm{CD8}}\frac{(\mathrm{CD8}(t) - \overline{\mathrm{CD8}})}{1 + |\mathrm{CD8}(t) - \overline{\mathrm{CD8}}|} - T_{\mathrm{T}}\mathrm{APC}^*(t)\, \mathrm{CD8}(t),$$
$$\mathrm{CD8}(t) = \overline{\mathrm{CD8}} \tag{32}$$

Active $\mathrm{CD8}^*$:

$$\frac{d}{dt}\mathrm{CD8}^*(t) = T_{\mathrm{T}}\mathrm{APC}^*(t)\, \mathrm{CD8}(t) - \lambda_{\mathrm{CD8}}\mathrm{CD8}^*(t),$$
$$\mathrm{CD8}^*(t) = 0 \tag{33}$$

Naïve B cells:

$$\frac{d}{dt}\mathrm{BC}(t) = -G_{\mathrm{BC}}\frac{(\mathrm{BC}(t) - \overline{\mathrm{BC}})}{1 + |\mathrm{BC}(t) - \overline{\mathrm{BC}}|} - T_{\mathrm{BC}}\mathrm{APC}^*(t)\, \mathrm{BC}(t), \qquad \mathrm{BC}(t) = \overline{\mathrm{BC}} \tag{34}$$

Activated B cells:

$$\frac{d}{dt}\mathrm{BC}^*(t) = T_{\mathrm{BC}}\mathrm{APC}^*(t)\, \mathrm{BC}(t) - (T^{\mathrm{S}}_{\mathrm{BC}} + T^{\mathrm{L}}_{\mathrm{BC}})\mathrm{CD4}^*(t)\, \mathrm{BC}^*(t),$$
$$\mathrm{BC}^*(t) = 0 \tag{35}$$

Activated B cells alone cannot neutralize the viral load. They must first transform into plasma cells, which then in turn produce antibodies that can carry out the viral neutralization. The transition from activated B cell to plasma cell is enabled by activated CD4* cells. This transformation can generate two types of plasma cells: short-lived (S) and long-lived (L). The transition rates are represented by the constants $T^{\mathrm{S}}_{\mathrm{BC}}$ and $T^{\mathrm{L}}_{\mathrm{BC}}$, and the corresponding concentrations of plasma cells are denoted by $\mathrm{P}^{\mathrm{S}}(t)$ and $\mathrm{P}^{\mathrm{L}}(t)$, respectively. Lastly, each type possesses a particular death rate, indicated by the constant $D^{\mathrm{S}}_{\mathrm{P}}$ for the short-lived type and $T^{\mathrm{L}}_{\mathrm{P}}$ for the long-lived type.

Naïve CD4:

$$\frac{d}{dt}\mathrm{CD4}(t) = -G_{\mathrm{CD4}}\frac{(\mathrm{CD4}(t) - \overline{\mathrm{CD4}})}{1 + |\mathrm{CD4}(t) - \overline{\mathrm{CD4}}|} - T_{\mathrm{T-cells}}\mathrm{APC}^*(t)\, \mathrm{CD4}(t),$$
$$\mathrm{CD4}(t) = \overline{\mathrm{CD4}} \tag{36}$$

https://dx.doi.org/10.1021/acsptsci.0c00183
ACS Pharmacol. Transl. Sci. 2021, 4, 248−265

Activated CD4:

$$\frac{d}{dt}\mathrm{CD4}^*(t) = T_{\mathrm{T-cells}}\mathrm{APC}^*(t)\mathrm{CD4}(t) - D_{\mathrm{CD4}}\mathrm{CD4}^*(t),$$
$$\mathrm{CD4}^*(t) = 0 \quad (37)$$

Short-lived plasma cells:

$$\frac{d}{dt}\mathrm{P}^{\mathrm{S}}(t) = T_{\mathrm{BC}}^{\mathrm{S}}\mathrm{CD4}^*(t)\ \mathrm{BC}^*(t) - D_{\mathrm{P}}^{\mathrm{S}}\mathrm{P}^{\mathrm{S}}(t),$$
$$\mathrm{P}^{\mathrm{S}}(t) = 0 \quad (38)$$

Long-lived plasma cells:

$$\frac{d}{dt}\mathrm{P}^{\mathrm{L}}(t) = T_{\mathrm{BC}}^{\mathrm{L}}\mathrm{CD4}^*(t)\ \mathrm{BC}^*(t) - D_{\mathrm{P}}^{\mathrm{L}}\mathrm{P}^{\mathrm{L}}(t),$$
$$\mathrm{P}^{\mathrm{L}}(t) = 0 \quad (39)$$

Antibodies:

$$\frac{d}{dt}\mathrm{Ab}(t) = G_{\mathrm{P}}^{\mathrm{S}}\mathrm{P}^{\mathrm{S}}(t) + G_{\mathrm{P}}^{\mathrm{L}}\mathrm{P}^{\mathrm{L}}(t) - \lambda_{\mathrm{Ab}}\mathrm{Ab}(t)\left(P(t) + \sum_{i\ \mathrm{in}\ \{U,L,I,M,H,K,B\}} v_i(t)\right) - \mathrm{Cl}_{\mathrm{Ab}}\mathrm{Ab}(t), \qquad \mathrm{Ab}(t) = 0 \quad (40)$$

The final equation in the model describes the rate of change of antibody concentration, $\mathrm{Ab}(t)$. The sole contributors to the production of antibodies are short-lived and long-lived plasma cells. The corresponding production rates are given by $G_{\mathrm{P}}^{\mathrm{S}}$ and $G_{\mathrm{P}}^{\mathrm{L}}$, respectively. We consider two mechanisms by which antibodies can be consumed or eliminated. One is the loss of antibodies due to their interaction with viral particles in a given compartment with rate constant λ_{Ab}. The second is the elimination of antibodies by other factors independent of the viral load, e.g., degradation or clearance from tissues, which occurs at rate constant $\mathrm{Cl}_{\mathrm{Ab}}$. A summary of the parameters used in the model is given in Tables 1−3.

Parametric Analysis. Once the full set of parameters for the model was defined and fixed for the conditions corresponding to Figure 4, we proceeded to identify the relative effect of each parameter on the viral kinetics. This was done by systematically perturbing multiple parameters simultaneously and comparing the outcomes between the perturbed state and the original state. To quantify the differences between the two states, we introduced the following six criteria. The first three refer to the area under the curve (AUC) of the viral load curves in the URT, the LRT, and the plasma compartment for a period of 30 days. Mathematically,

$$\mathrm{AUC}_i = \int_0^{30} v_i(t)dt, \text{ for } i \text{ in } \{U, L, P\}$$

The next three denote the total time required for the viral load in the URT, LRT, and plasma compartment to reduce to $<10^2$ viral copies per mL, i.e., 2 in log base 10 units. In the next subsection, we compare each of the 6 criteria using global sensitivity analysis (GSA), applied to the 31 parameters.

Global Sensitivity Analysis. Local sensitivity analysis only allows one parameter to change at a time and thus may not shed light on the effect of parameter interactions in complex biological systems. Thus, we performed global sensitivity analysis (GSA;[39,65−67] i.e., multiple parameters can be varied simultaneously) to obtain a further understanding of the relationship between parameters and their combined effects on the model outputs of interest. Specifically, in our analysis, all parameters were perturbed at the same time, and we assumed a uniform distribution of values for each parameter. The range of values of each sample was PR ± 99% of PR, where PR is the reference value of a given parameter. To ensure comprehensive sampling of the multidimensional parameter space, we used a Latin hypercube sampling scheme. Subsequently, each sample (made up of 31 parameter values) was used to compute the kinetics, from which we extracted the 6 criteria mentioned above. In total, 10 batches of 5000 samples each were computed. Then, each batch was subjected to a multivariate linear regression analysis to obtain the regression coefficients of the parameters, and then averaging the regression coefficients of each parameter over 10 batches, we obtained the mean and variance of the sensitivity index (SI) for each parameter. Lastly, the sensitivity indices were ranked by means of a one-way ANOVA and a Tukey's test. The higher the SI, the more significance a parameter holds. A detailed description of the GSA workflow can be found in refs 39 and 65−67. All analyses were performed in MATLAB R2018a.

■ ASSOCIATED CONTENT

Supporting Information

The Supporting Information is available free of charge at https://pubs.acs.org/doi/10.1021/acsptsci.0c00183.

Pearson correlation of model predictions to experimental data (PDF)

■ AUTHOR INFORMATION

Corresponding Authors

Prashant Dogra − *Mathematics in Medicine Program, Houston Methodist Research Institute, Houston, Texas 77030, United States*; Email: pdogra@houstonmethodist.org

Zhihui Wang − *Mathematics in Medicine Program, Houston Methodist Research Institute, Houston, Texas 77030, United States; Weill Cornell Medicine, New York 10065, United States*; orcid.org/0000-0001-6262-700X; Email: zwang@houstonmethodist.org

Authors

Javier Ruiz-Ramírez − *Mathematics in Medicine Program, Houston Methodist Research Institute, Houston, Texas 77030, United States*

Kavya Sinha − *DeBakey Heart and Vascular Center, Houston Methodist Hospital, Houston, Texas 77030, United States*

Joseph D. Butner − *Mathematics in Medicine Program, Houston Methodist Research Institute, Houston, Texas 77030, United States*

Maria J. Peláez − *Mathematics in Medicine Program, Houston Methodist Research Institute, Houston, Texas 77030, United States*

Manmeet Rawat − *Department of Internal Medicine, University of New Mexico School of Medicine, Albuquerque, New Mexico 87131, United States*

Venkata K. Yellepeddi − *Division of Clinical Pharmacology, Department of Pediatrics, School of Medicine and Department of Pharmaceutics and Pharmaceutical Chemistry, College of Pharmacy, University of Utah, Salt Lake City, Utah 84132, United States*

https://dx.doi.org/10.1021/acsptsci.0c00183
ACS Pharmacol. Transl. Sci. 2021, 4, 248−265

Renata Pasqualini − *Rutgers Cancer Institute of New Jersey, Newark, New Jersey 07101, United States; Department of Radiation Oncology, Division of Cancer Biology, Rutgers New Jersey Medical School, Newark, New Jersey 07103, United States*

Wadih Arap − *Rutgers Cancer Institute of New Jersey, Newark, New Jersey 07101, United States; Department of Medicine, Division of Hematology/Oncology, Rutgers New Jersey Medical School, Newark, New Jersey 07103, United States*

H. Dirk Sostman − *Weill Cornell Medicine, New York 10065, United States; Houston Methodist Research Institute, Houston, Texas 77030, United States; Houston Methodist Academic Institute, Houston, Texas 77030, United States*

Vittorio Cristini − *Mathematics in Medicine Program, Houston Methodist Research Institute, Houston, Texas 77030, United States; Weill Cornell Medicine, New York 10065, United States*

Complete contact information is available at: https://pubs.acs.org/10.1021/acsptsci.0c00183

Author Contributions

[&]JRR, KS, and JDB contributed equally. PD and ZW conceived the study, conceptualized the idea, and designed the model. PD and JRR developed the model. PD, JRR, KS, MJP, and MR collected the data. PD, KS, JDB, VKY, RP, WA, MB, DS, VC, and ZW interpreted the data. PD, JRR, JDB, and ZW performed the model analysis. PD, JRR, KS, JDB, MJP, MR, RP, WA, DS, VC, and ZW wrote or edited the manuscript.

Notes

The authors declare no competing financial interest.

■ ACKNOWLEDGMENTS

This research has been supported in part by the National Science Foundation Grant DMS-1930583 (VC, ZW) and the National Institutes of Health (NIH) Grants 1U01CA196403 (VC, ZW), 1U01CA213759 (VC, ZW), 1R01CA226537 (RP, WA, VC, ZW), 1R01CA222007 (VC, ZW), and U54CA210181 (VC, ZW). The funders had no role in study design, data collection and analysis, decision to publish, or preparation of the manuscript.

■ REFERENCES

(1) Medicine, J. H. U. Coronavirus Resource Center https://coronavirus.jhu.edu/map.html (accessed 2020-11-27).

(2) Evans, O. (2020) Socio-economic impacts of novel coronavirus: The policy solutions. *BizEcons Quarterly 7*, 3−12.

(3) Barry, M., Al Amri, M., and Memish, Z. A. (2020) COVID-19 in the shadows of MERS-CoV in the Kingdom of Saudi Arabia. *J. Epidemiol Glob Health 10* (1), 1−3.

(4) Wrapp, D., Wang, N., Corbett, K. S., Goldsmith, J. A., Hsieh, C.-L., Abiona, O., Graham, B. S., and McLellan, J. S. (2020) Cryo-EM structure of the 2019-nCoV spike in the prefusion conformation. *Science 367* (6483), 1260−1263.

(5) Hamming, I., Timens, W., Bulthuis, M., Lely, A., Navis, G., and van Goor, H. (2004) Tissue distribution of ACE2 protein, the functional receptor for SARS coronavirus. A first step in understanding SARS pathogenesis. *J. Pathol. 203* (2), 631−637.

(6) To, K. K.-W., Tsang, O. T.-Y., Leung, W.-S., Tam, A. R., Wu, T.-C., Lung, D. C., Yip, C. C.-Y., Cai, J.-P., Chan, J. M.-C., and Chik, T. S.-H. (2020) Temporal profiles of viral load in posterior oropharyngeal saliva samples and serum antibody responses during infection by SARS-CoV-2: An observational cohort study. *Lancet Infect Dis*.

(7) Wang, Y., Heiland, R., Craig, M., Davis, C. L., Versypt, A. N. F., Jenner, A., Ozik, J., Collier, N., Cockrell, C., and Becker, A. (2020) Rapid community-driven development of a SARS-CoV-2 tissue simulator. *BioRxiv*. DOI: 10.1101/2020.04.02.019075.

(8) Zitzmann, C., and Kaderali, L. (2018) Mathematical analysis of viral replication dynamics and antiviral treatment strategies: From basic models to age-based multi-scale modeling. *Front. Microbiol. 9*, 1546.

(9) Hancioglu, B., Swigon, D., and Clermont, G. (2007) A dynamical model of human immune response to influenza A virus infection. *J. Theor. Biol. 246* (1), 70−86.

(10) Baccam, P., Beauchemin, C., Macken, C. A., Hayden, F. G., and Perelson, A. S. (2006) Kinetics of influenza A virus infection in humans. *J. Virol. 80* (15), 7590−7599.

(11) Lee, H. Y., Topham, D. J., Park, S. Y., Hollenbaugh, J., Treanor, J., Mosmann, T. R., Jin, X., Ward, B. M., Miao, H., and Holden-Wiltse, J. (2009) Simulation and prediction of the adaptive immune response to influenza A virus infection. *J. Virol. 83* (14), 7151−7165.

(12) Layden, T. J., Layden, J. E., Ribeiro, R. M., and Perelson, A. S. (2003) Mathematical modeling of viral kinetics: A tool to understand and optimize therapy. *Clin Liver Dis 7* (1), 163−178.

(13) Koelle, K., Farrell, A. P., Brooke, C. B., and Ke, R. (2019) Within-host infectious disease models accommodating cellular coinfection, with an application to influenza. *Virus Evol 5* (2), No. vez018.

(14) Kucharski, A. J., Russell, T. W., Diamond, C., Liu, Y., Edmunds, J., Funk, S., Eggo, R. M., Sun, F., Jit, M., and Munday, J. D. (2020) Early dynamics of transmission and control of COVID-19: A mathematical modelling study. *Lancet Infect Dis*.

(15) Berhe, B., Legese, H., Degefa, H., Adhanom, G., Gebrewahd, A., Mardu, F., Tesfay, K., Welay, M., and Negash, H. (2020) Global epidemiology, pathogenesis, immune response, diagnosis, treatment, economic and psychological impact, challenges, and future prevention of COVID-19: A scoping review. *medRxiv* DOI: 10.1101/2020.04.02.20051052.

(16) Eletreby, R., Zhuang, Y., Carley, K. M., Yağan, O., and Poor, H. V. (2020) The effects of evolutionary adaptations on spreading processes in complex networks. *Proc. Natl. Acad. Sci. U. S. A. 117* (11), 5664−5670.

(17) Zhao, S., Lin, Q., Ran, J., Musa, S. S., Yang, G., Wang, W., Lou, Y., Gao, D., Yang, L., and He, D. (2020) Preliminary estimation of the basic reproduction number of novel coronavirus (2019-nCoV) in China, from 2019 to 2020: A data-driven analysis in the early phase of the outbreak. *Int. J. Infect. Dis. 92*, 214−217.

(18) Wu, J. T., Leung, K., and Leung, G. M. (2020) Nowcasting and forecasting the potential domestic and international spread of the 2019-nCoV outbreak originating in Wuhan, China: A modelling study. *Lancet 395* (10225), 689−697.

(19) Goyal, A., Cardozo-Ojeda, E. F., and Schiffer, J. T. (2020) Potency and timing of antiviral therapy as determinants of duration of SARS CoV-2 shedding and intensity of inflammatory response. *Sci. Adv. 6* (47), No. eabc7112.

(20) Perelson, A. S., Neumann, A. U., Markowitz, M., Leonard, J. M., and Ho, D. D. (1996) HIV-1 dynamics in vivo: Virion clearance rate, infected cell life-span, and viral generation time. *Science 271* (5255), 1582−1586.

(21) Sahoo, S., Hari, K., Jhunjhunwala, S., and Jolly, M. K. (2020) Mechanistic modeling of the SARS-CoV-2 and immune system interplay unravels design principles for diverse clinicopathological outcomes. *bioRxiv* DOI: 10.1101/2020.05.16.097238.

(22) Ke, R., Zitzmann, C., Ribeiro, R. M., and Perelson, A. S. (2020) Kinetics of SARS-CoV-2 infection in the human upper and lower respiratory tracts and their relationship with infectiousness. *medRxiv* DOI: 10.1101/2020.09.25.20201772.

(23) Puelles, V. G., Lütgehetmann, M., Lindenmeyer, M. T., Sperhake, J. P., Wong, M. N., Allweiss, L., Chilla, S., Heinemann, A., Wanner, N., Liu, S., Braun, F., Lu, S., Pfefferle, S., Schröder, A. S., Edler, C., Gross, O., Glatzel, M., Wichmann, D., Wiech, T., Kluge, S.,

Pueschel, K., Aepfelbacher, M., and Huber, T. B. (2020) Multiorgan and renal tropism of SARS-CoV-2. *N. Engl. J. Med. 383* (6), 590−592.
(24) Zou, X., Chen, K., Zou, J., Han, P., Hao, J., and Han, Z. (2020) Single-cell RNA-seq data analysis on the receptor ACE2 expression reveals the potential risk of different human organs vulnerable to 2019-nCoV infection. *Front Med. 14*, 1−8.
(25) Ziegler, C. G., Allon, S. J., Nyquist, S. K., Mbano, I. M., Miao, V. N., Tzouanas, C. N., Cao, Y., Yousif, A. S., Bals, J., and Hauser, B. M. (2020) SARS-CoV-2 receptor ACE2 is an interferon-stimulated gene in human airway epithelial cells and is detected in specific cell subsets across tissues. *Cell*.
(26) Harmer, D., Gilbert, M., Borman, R., and Clark, K. L. (2002) Quantitative mRNA expression profiling of ACE 2, a novel homologue of angiotensin converting enzyme. *FEBS Lett. 532* (1−2), 107−10.
(27) Kim, J.-M., Kim, H. M., Lee, E. J., Jo, H. J., Yoon, Y., Lee, N.-J., Son, J., Lee, Y.-J., Kim, M. S., Lee, Y.-P., Chae, S.-J., Park, K. R., Cho, S.-R., Park, S., Kim, S. J., Wang, E., Woo, S., Lim, A., Park, S.-J., Jang, J., Chung, Y.-S., Chin, B. S., Lee, J.-S., Lim, D., Han, M.-G., and Yoo, C. K. (2020) Detection and isolation of SARS-CoV-2 in serum, urine, and stool specimens of COVID-19 patients from the Republic of Korea. *Osong Public Health Res. Perspect 11* (3), 112−117.
(28) Jothimani, D., Venugopal, R., Abedin, M. F., Kaliamoorthy, I., and Rela, M. (2020) COVID-19 and Liver. *J. Hepatol.*
(29) Zhang, C., Shi, L., and Wang, F.-S. (2020) Liver injury in COVID-19: Management and challenges. *Lancet Gastroenterol Hepatol 5* (5), 428−430.
(30) Chan, J. F.-W., Zhang, A. J., Yuan, S., Poon, V. K.-M., Chan, C. C.-S., Lee, A. C.-Y., Chan, W.-M., Fan, Z., Tsoi, H.-W., and Wen, L. (2020) Simulation of the clinical and pathological manifestations of Coronavirus Disease 2019 (COVID-19) in golden Syrian hamster model: Implications for disease pathogenesis and transmissibility. *Clin Infect Dis*.
(31) Vetter, P., Eberhardt, C. S., Meyer, B., Murillo, P. A. M., Torriani, G., Pigny, F., Lemeille, S., Cordey, S., Laubscher, F., and Vu, D.-L. (2020) Daily viral kinetics and innate and adaptive immune response assessment in COVID-19: A case series. *Msphere 5* (6).
(32) Bastard, P., Rosen, L. B., Zhang, Q., Michailidis, E., Hoffmann, H.-H., Zhang, Y., Dorgham, K., Philippot, Q., Rosain, J., Béziat, V., Manry, J., Shaw, E., Haljasmägi, L., Peterson, P., Lorenzo, L., Bizien, L., Trouillet-Assant, S., Dobbs, K., de Jesus, A. A., Belot, A., Kallaste, A., Catherinot, E., Tandjaoui-Lambiotte, Y., Le Pen, J., Kerner, G., Bigio, B., Seeleuthner, Y., Yang, R., Bolze, A., Spaan, A. N., Delmonte, O. M., Abers, M. S., Aiuti, A., Casari, G., Lampasona, V., Piemonti, L., Ciceri, F., Bilguvar, K., Lifton, R. P., Vasse, M., Smadja, D. M., Migaud, M., Hadjadj, J., Terrier, B., Duffy, D., Quintana-Murci, L., van de Beek, D., Roussel, L., Vinh, D. C., Tangye, S. G., Haerynck, F., Dalmau, D., Martinez-Picado, J., Brodin, P., Nussenzweig, M. C., Boisson-Dupuis, S., Rodríguez-Gallego, C., Vogt, G., Mogensen, T. H., Oler, A. J., Gu, J., Burbelo, P. D., Cohen, J., Biondi, A., Bettini, L. R., D'Angio, M., Bonfanti, P., Rossignol, P., Mayaux, J., Rieux-Laucat, F., Husebye, E. S., Fusco, F., Ursini, M. V., Imberti, L., Sottini, A., Paghera, S., Quiros-Roldan, E., Rossi, C., Castagnoli, R., Montagna, D., Licari, A., Marseglia, G. L., Duval, X., Ghosn, J., Tsang, J. S., Goldbach-Mansky, R., Kisand, K., Lionakis, M. S., Puel, A., Zhang, S.-Y., Holland, S. M., Gorochov, G., Jouanguy, E., Rice, C. M., Cobat, A., Notarangelo, L. D., Abel, L., Su, H. C., and Casanova, J.-L. (2020) Auto-antibodies against type I IFNs in patients with life-threatening COVID-19. *Science 370*, No. eabd4585.
(33) Zhang, Q., Bastard, P., Liu, Z., Le Pen, J., Moncada-Velez, M., Chen, J., Ogishi, M., Sabli, I. K. D., Hodeib, S., Korol, C., Rosain, J., Bilguvar, K., Ye, J., Bolze, A., Bigio, B., Yang, R., Arias, A. A., Zhou, Q., Zhang, Y., Onodi, F., Korniotis, S., Karpf, L., Philippot, Q., Chbihi, M., Bonnet-Madin, L., Dorgham, K., Smith, N., Schneider, W. M., Razooky, B. S., Hoffmann, H.-H., Michailidis, E., Moens, L., Han, J. E., Lorenzo, L., Bizien, L., Meade, P., Neehus, A.-L., Ugurbil, A. C., Corneau, A., Kerner, G., Zhang, P., Rapaport, F., Seeleuthner, Y., Manry, J., Masson, C., Schmitt, Y., Schlüter, A., Le Voyer, T., Khan, T., Li, J., Fellay, J., Roussel, L., Shahrooei, M., Alosaimi, M. F., Mansouri, D., Al-Saud, H., Al-Mulla, F., Almourfi, F., Al-Muhsen, S. Z., Alsohime, F., Al Turki, S., Hasanato, R., van de Beek, D., Biondi, A., Bettini, L. R., D'Angio, M., Bonfanti, P., Imberti, L., Sottini, A., Paghera, S., Quiros-Roldan, E., Rossi, C., Oler, A. J., Tompkins, M. F., Alba, C., Vandernoot, I., Goffard, J.-C., Smits, G., Migeotte, I., Haerynck, F., Soler-Palacin, P., Martin-Nalda, A., Colobran, R., Morange, P.-E., Keles, S., Çölkesen, F., Ozcelik, T., Yasar, K. K., Senoglu, S., Karabela, Ş. N., Gallego, C. R., Novelli, G., Hraiech, S., Tandjaoui-Lambiotte, Y., Duval, X., Laouénan, C., Snow, A. L., Dalgard, C. L., Milner, J., Vinh, D. C., Mogensen, T. H., Marr, N., Spaan, A. N., Boisson, B., Boisson-Dupuis, S., Bustamante, J., Puel, A., Ciancanelli, M., Meyts, I., Maniatis, T., Soumelis, V., Amara, A., Nussenzweig, M., García-Sastre, A., Krammer, F., Pujol, A., Duffy, D., Lifton, R., Zhang, S.-Y., Gorochov, G., Béziat, V., Jouanguy, E., Sancho-Shimizu, V., Rice, C. M., Abel, L., Notarangelo, L. D., Cobat, A., Su, H. C., and Casanova, J.-L. (2020) Inborn errors of type I IFN immunity in patients with life-threatening COVID-19. *Science 370*, No. eabd4570.
(34) Hadjadj, J., Yatim, N., Barnabei, L., Corneau, A., Boussier, J., Pere, H., Charbit, B., Bondet, V., Chenevier-Gobeaux, C., and Breillat, P. (2020) Impaired type I interferon activity and exacerbated inflammatory responses in severe Covid-19 patients. *Science 369* (6504), 718−724.
(35) Fenner, F., Bachmann, P. A., Gibbs, E. P. J., Murphy, F. A., Studdert, M. J., and White, D. O. (1987) Pathogenesis: Infection and the spread of viruses in the body. *Vet Virol*, 133.
(36) Dogra, P., Adolphi, N. L., Wang, Z., Lin, Y.-S., Butler, K. S., Durfee, P. N., Croissant, J. G., Noureddine, A., Coker, E. N., Bearer, E. L., Cristini, V., and Brinker, C. J. (2018) Establishing the effects of mesoporous silica nanoparticle properties on in vivo disposition using imaging-based pharmacokinetics. *Nat. Commun. 9* (1), 4551.
(37) Dogra, P., Butner, J. D., Chuang, Y.-l., Caserta, S., Goel, S., Brinker, C. J., Cristini, V., and Wang, Z. (2019) Mathematical modeling in cancer nanomedicine: A review. *Biomed. Microdevices 21* (2), 40.
(38) Dogra, P., Butner, J. D., Nizzero, S., Ruiz Ramirez, J., Noureddine, A., Pelaez, M. J., Elganainy, D., Yang, Z., Le, A. D., Goel, S., Leong, H. S., Koay, E. J., Brinker, C. J., Cristini, V., and Wang, Z. (2020) Image-guided mathematical modeling for pharmacological evaluation of nanomaterials and monoclonal antibodies. *Wiley Interdiscip. Rev.: Nanomed. Nanobiotechnol. 12*, No. e1628.
(39) Dogra, P., Butner, J. D., Ramírez, J. R., Chuang, Y.-l., Noureddine, A., Brinker, C. J., Cristini, V., and Wang, Z. (2020) A mathematical model to predict nanomedicine pharmacokinetics and tumor delivery. *Comput. Struct. Biotechnol. J. 18*, 518−531.
(40) Cristini, V., Koay, E., and Wang, Z. (2017) *An Introduction to Physical Oncology: How Mechanistic Mathematical Modeling Can. Improve Cancer Therapy Outcomes*, CRC Press, p 164.
(41) Wang, Z., Kerketta, R., Chuang, Y. L., Dogra, P., Butner, J. D., Brocato, T. A., Day, A., Xu, R., Shen, H., Simbawa, E., Al-Fhaid, A. S., Mahmoud, S. R., Curley, S. A., Ferrari, M., Koay, E. J., and Cristini, V. (2016) Theory and experimental validation of a spatio-temporal model of chemotherapy transport to enhance tumor cell kill. *PLoS Comput. Biol. 12* (6), No. e1004969.
(42) Brocato, T. A., Coker, E. N., Durfee, P. N., Lin, Y. S., Townson, J., Wyckoff, E. F., Cristini, V., Brinker, C. J., and Wang, Z. (2018) Understanding the connection between nanoparticle uptake and cancer treatment efficacy using mathematical modeling. *Sci. Rep. 8* (1), 7538.
(43) Goel, S., Ferreira, C. A., Dogra, P., Yu, B., Kutyreff, C. J., Siamof, C. M., Engle, J. W., Barnhart, T. E., Cristini, V., and Wang, Z. (2019) Size-optimized ultrasmall porous silica nanoparticles depict vasculature-based differential targeting in triple Nnegative breast cancer. *Small*.
(44) Goel, S., Zhang, G., Dogra, P., Nizzero, S., Cristini, V., Wang, Z., Hu, Z., Li, Z., Liu, X., and Shen, H. (2020) Sequential deconstruction of composite drug transport in metastatic breast cancer. *Sci. Adv. 6* (26), No. eaba4498.

https://dx.doi.org/10.1021/acsptsci.0c00183
ACS Pharmacol. Transl. Sci. 2021, 4, 248−265

(45) Sarin, H. (2010) Physiologic upper limits of pore size of different blood capillary types and another perspective on the dual pore theory of microvascular permeability. *J. Angiog. Res. 2* (1), 14.
(46) Qin, J., You, C., Lin, Q., Hu, T., Yu, S., and Zhou, X.-H. (2020) Estimation of incubation period distribution of COVID-19 using disease onset forward time: A novel cross-sectional and forward follow-up study. *Sci. Adv. 6* (33), No. eabc1202, *medRxiv* **2020**..
(47) Zheng, S., Fan, J., Yu, F., Feng, B., Lou, B., Zou, Q., Xie, G., Lin, S., Wang, R., and Yang, X. (2020) Viral load dynamics and disease severity in patients infected with SARS-CoV-2 in Zhejiang province, China, January-March 2020: Retrospective cohort study. *Br Med. J. 369*.
(48) Iyer, A. S., Jones, F. K., Nodoushani, A., Kelly, M., Becker, M., Slater, D., Mills, R., Teng, E., Kamruzzaman, M., and Garcia-Beltran, W. F. (2020) Persistence and decay of human antibody responses to the receptor binding domain of SARS-CoV-2 spike protein in COVID-19 patients. *Sci. Immunol 5* (52).
(49) Isho, B., Abe, K. T., Zuo, M., Jamal, A. J., Rathod, B., Wang, J. H., Li, Z., Chao, G., Rojas, O. L., and Bang, Y. M. (2020) Persistence of serum and saliva antibody responses to SARS-CoV-2 spike antigens in COVID-19 patients. *Sci. Immunol 5* (52).
(50) Tillett, R. L., Sevinsky, J. R., Hartley, P. D., Kerwin, H., Crawford, N., Gorzalski, A., Laverdure, C., Verma, S. C., Rossetto, C. C., and Jackson, D. (2020) Genomic evidence for reinfection with SARS-CoV-2: A case study. *Lancet Infect Dis*.
(51) Seow, J., Graham, C., Merrick, B., Acors, S., Pickering, S., Steel, K. J. A., Hemmings, O., O'Byrne, A., Kouphou, N., Galao, R. P., Betancor, G., Wilson, H. D., Signell, A. W., Winstone, H., Kerridge, C., Huettner, I., Jimenez-Guardeño, J. M., Lista, M. J., Temperton, N., Snell, L. B., Bisnauthsing, K., Moore, A., Green, A., Martinez, L., Stokes, B., Honey, J., Izquierdo-Barras, A., Arbane, G., Patel, A., Tan, M. K. I., O'Connell, L., O'Hara, G., MacMahon, E., Douthwaite, S., Nebbia, G., Batra, R., Martinez-Nunez, R., Shankar-Hari, M., Edgeworth, J. D., Neil, S. J. D., Malim, M. H., and Doores, K. J. (2020) Longitudinal observation and decline of neutralizing antibody responses in the three months following SARS-CoV-2 infection in humans. *Nat. Microbiol.*
(52) Gupta, A., Madhavan, M. V., Sehgal, K., Nair, N., Mahajan, S., Sehrawat, T. S., Bikdeli, B., Ahluwalia, N., Ausiello, J. C., and Wan, E. Y. (2020) Extrapulmonary manifestations of COVID-19. *Nat. Med. 26* (7), 1017−1032.
(53) Cai, X., Ma, Y., Li, S., Chen, Y., Rong, Z., and Li, W. (2020) Clinical characteristics of 5 COVID-19 cases With non-respiratory symptoms as the first manifestation in children. *Front Pediatr 8*, 258.
(54) Tavazzi, G., Pellegrini, C., Maurelli, M., Belliato, M., Sciutti, F., Bottazzi, A., Sepe, P. A., Resasco, T., Camporotondo, R., and Bruno, R. (2020) Myocardial localization of coronavirus in COVID-19 cardiogenic shock. *Eur. J. Heart Fail.*
(55) Puelles, V. G., Lütgehetmann, M., Lindenmeyer, M. T., Sperhake, J. P., Wong, M. N., Allweiss, L., Chilla, S., Heinemann, A., Wanner, N., and Liu, S. (2020) Multiorgan and renal tropism of SARS-CoV-2. *New Engl J. Med.*
(56) Wichmann, D., Sperhake, J.-P., Lütgehetmann, M., Steurer, S., Edler, C., Heinemann, A., Heinrich, F., Mushumba, H., Kniep, I., and Schröder, A. S. (2020) Autopsy findings and venous thromboembolism in patients with COVID-19: A prospective cohort study. *Ann. Intern. Med.*
(57) Liao, M., Liu, Y., Yuan, J., Wen, Y., Xu, G., Zhao, J., Chen, L., Li, J., Wang, X., and Wang, F. (2020) The landscape of lung bronchoalveolar immune cells in COVID-19 revealed by single-cell RNA sequencing. *Nat. Med. 26*, 842−844.
(58) Perea, L., Rodrigo-Troyano, A., Cantó, E., Domínguez-Álvarez, M., Giner, J., Sanchez-Reus, F., Villar-García, J., Quero, S., García-Núñez, M., and Marín, A. (2020) Reduced airway levels of fatty-acid binding protein 4 in COPD: relationship with airway infection and disease severity. *Respir. Res. 21* (1), 1−8.
(59) Chen, Y., Feng, Z., Diao, B., Wang, R., Wang, G., Wang, C., Tan, Y., and Yuan, Z. (2020) The novel severe acute respiratory syndrome coronavirus 2 (SARS-CoV-2) directly decimates human spleens and lymph nodes. *medRxiv* DOI: 10.1101/2020.03.27.20045427.
(60) Sanders, J. M., Monogue, M. L., Jodlowski, T. Z., and Cutrell, J. B. (2020) Pharmacologic treatments for coronavirus disease 2019 (COVID-19): a review. *JAMA 323* (18), 1824−1836.
(61) Beigel, J. H., Tomashek, K. M., Dodd, L. E., Mehta, A. K., Zingman, B. S., Kalil, A. C., Hohmann, E., Chu, H. Y., Luetkemeyer, A., Kline, S., Lopez de Castilla, D., Finberg, R. W., Dierberg, K., Tapson, V., Hsieh, L., Patterson, T. F., Paredes, R., Sweeney, D. A., Short, W. R., Touloumi, G., Lye, D. C., Ohmagari, N., Oh, M.-d., Ruiz-Palacios, G. M., Benfield, T., Fätkenheuer, G., Kortepeter, M. G., Atmar, R. L., Creech, C. B., Lundgren, J., Babiker, A. G., Pett, S., Neaton, J. D., Burgess, T. H., Bonnett, T., Green, M., Makowski, M., Osinusi, A., Nayak, S., and Lane, H. C. (2020) Remdesivir for the treatment of Covid-19 — Final report. *New Engl J. Med.*
(62) Hu, X., Shang, S., Nestorov, I., Hasan, J., Seddighzadeh, A., Dawson, K., Sperling, B., and Werneburg, B. (2016) COMPARE: Pharmacokinetic profiles of subcutaneous peginterferon beta-1a and subcutaneous interferon beta-1a over 2 weeks in healthy subjects. *Br. J. Clin. Pharmacol. 82* (2), 380−388.
(63) Bar-On, Y. M., Flamholz, A., Phillips, R., and Milo, R. (2020) SARS-CoV-2 (COVID-19) by the numbers. *eLife 9*, No. e57309.
(64) Pezzini, A., and Padovani, A. (2020) Lifting the mask on neurological manifestations of COVID-19. *Nat. Rev. Neurol. 16*, 1−9.
(65) Wang, Z., Bordas, V., and Deisboeck, T. S. (2011) Identification of critical molecular components in a multiscale cancer model based on the integration of Monte Carlo, resampling, and ANOVA. *Front. Physiol. 2*, 35−35.
(66) Wang, Z., Deisboeck, T. S., and Cristini, V. (2014) Development of a sampling-based global sensitivity analysis workflow for multiscale computational cancer models. *IET Syst. Biol. 8* (5), 191−7.
(67) Butner, J. D., Fuentes, D., Ozpolat, B., Calin, G. A., Zhou, X., Lowengrub, J., Cristini, V., and Wang, Z. (2020) A Multiscale agent-based model of ductal carcinoma in situ. *IEEE Trans. Biomed. Eng. 67* (5), 1450−1461.
(68) De Boer, R. J., and Perelson, A. S. (2013) Quantifying T lymphocyte turnover. *J. Theor. Biol. 327*, 45−87.
(69) Westera, L., Drylewicz, J., den Braber, I., Mugwagwa, T., van der Maas, I., Kwast, L., Volman, T., van de Weg-Schrijver, E. H., Bartha, I., Spierenburg, G., Gaiser, K., Ackermans, M. T., Asquith, B., de Boer, R. J., Tesselaar, K., and Borghans, J. A. (2013) Closing the gap between T-cell life span estimates from stable isotope-labeling studies in mice and humans. *Blood 122* (13), 2205−12.
(70) Auner, H. W., Beham-Schmid, C., Dillon, N., and Sabbattini, P. (2010) The life span of short-lived plasma cells is partly determined by a block on activation of apoptotic caspases acting in combination with endoplasmic reticulum stress. *Blood 116* (18), 3445−3455.
(71) Andraud, M., Lejeune, O., Musoro, J. Z., Ogunjimi, B., Beutels, P., and Hens, N. (2012) Living on three time scales: the dynamics of plasma cell and antibody populations illustrated for hepatitis a virus. *PLoS Comput. Biol. 8* (3), No. e1002418-e1002418.
(72) Bortnick, A., and Allman, D. (2013) What is and what should always have been: long-lived plasma cells induced by T cell-independent antigens. *J. Immunol. 190* (12), 5913−5918.
(73) Kumar, B. V., Connors, T. J., and Farber, D. L. (2018) Human T cell development, localization, and function throughout life. *Immunity 48* (2), 202−213.
(74) Collin, M., and Bigley, V. (2018) Human dendritic cell subsets: An update. *Immunology 154* (1), 3−20.
(75) Gray, D. (1998) Lifespan of immune cells and molecules. In *Encyclopedia of Immunology* (Delves, P. J., Ed.) 2nd ed., pp 1579−1583, Elsevier, Oxford.
(76) Alloatti, A., Kotsias, F., Magalhaes, J. G., and Amigorena, S. (2016) Dendritic cell maturation and cross-presentation: timing matters! *Immunol Rev. 272* (1), 97−108.
(77) Nair, S., Archer, G. E., and Tedder, T. F. (2012) Isolation and generation of human dendritic cells. *Curr. Protoc. Immunol.* Chapter 7, Unit 7.32.

(78) Bianconi, E., Piovesan, A., Facchin, F., Beraudi, A., Casadei, R., Frabetti, F., Vitale, L., Pelleri, M. C., Tassani, S., Piva, F., Perez-Amodio, S., Strippoli, P., and Canaider, S. (2013) An estimation of the number of cells in the human body. *Ann. Hum. Biol. 40* (6), 463−71.
(79) Bittersohl, H., and Steimer, W. (2016) Chapter 9 - Intracellular concentrations of immunosuppressants. In *Personalized Immunosuppression in Transplantation* (Oellerich, M., and Dasgupta, A., Eds.), pp 199−226, Elsevier, San Diego.
(80) Alberts, B., Johnson, A., Lewis, J., Raff, M., Roberts, K., and Walter, P. (2002) *Mol. Biol. Cell*, 4th ed. Garland Science, New York.
(81) Ruedl, C., Koebel, P., Bachmann, M., Hess, M., and Karjalainen, K. (2000) Anatomical origin of dendritic cells determines their life span in peripheral lymph nodes. *J. Immunol. 165* (9), 4910−4916.
(82) Macallan, D. C., Wallace, D. L., Zhang, Y., Ghattas, H., Asquith, B., de Lara, C., Worth, A., Panayiotakopoulos, G., Griffin, G. E., Tough, D. F., and Beverley, P. C. L. (2005) B-cell kinetics in humans: Rapid turnover of peripheral blood memory cells. *Blood 105* (9), 3633−3640.
(83) Benson, N., de Jongh, J., Duckworth, J. D., Jones, H. M., Pertinez, H. E., Rawal, J. K., van Steeg, T. J., and Van der Graaf, P. H. (2010) Pharmacokinetic-pharmacodynamic modeling of alpha interferon response induced by a Toll-like 7 receptor agonist in mice. *Antimicrob. Agents Chemother. 54* (3), 1179−1185.
(84) Ziegler, C. G. K., Allon, S. J., Nyquist, S. K., Mbano, I. M., Miao, V. N., Tzouanas, C. N., Cao, Y., Yousif, A. S., Bals, J., Hauser, B. M., Feldman, J., Muus, C., Wadsworth, M. H., Kazer, S. W., Hughes, T. K., Doran, B., Gatter, G. J., Vukovic, M., Taliaferro, F., Mead, B. E., Guo, Z., Wang, J. P., Gras, D., Plaisant, M., Ansari, M., Angelidis, I., Adler, H., Sucre, J. M. S., Taylor, C. J., Lin, B., Waghray, A., Mitsialis, V., Dwyer, D. F., Buchheit, K. M., Boyce, J. A., Barrett, N. A., Laidlaw, T. M., Carroll, S. L., Colonna, L., Tkachev, V., Peterson, C. W., Yu, A., Zheng, H. B., Gideon, H. P., Winchell, C. G., Lin, P. L., Bingle, C. D., Snapper, S. B., Kropski, J. A., Theis, F. J., Schiller, H. B., Zaragosi, L.-E., Barbry, P., Leslie, A., Kiem, H.-P., Flynn, J. L., Fortune, S. M., Berger, B., Finberg, R. W., Kean, L. S., Garber, M., Schmidt, A. G., Lingwood, D., Shalek, A. K., Ordovas-Montanes, J., Banovich, N., Barbry, P., Brazma, A., Desai, T., Duong, T. E., Eickelberg, O., Falk, C., Farzan, M., Glass, I., Haniffa, M., Horvath, P., Hung, D., Kaminski, N., Krasnow, M., Kropski, J. A., Kuhnemund, M., Lafyatis, R., Lee, H., Leroy, S., Linnarson, S., Lundeberg, J., Meyer, K., Misharin, A., Nawijn, M., Nikolic, M. Z., Ordovas-Montanes, J., Pe'er, D., Powell, J., Quake, S., Rajagopal, J., Tata, P. R., Rawlins, E. L., Regev, A., Reyfman, P. A., Rojas, M., Rosen, O., Saeb-Parsy, K., Samakovlis, C., Schiller, H., Schultze, J. L., Seibold, M. A., Shalek, A. K., Shepherd, D., Spence, J., Spira, A., Sun, X., Teichmann, S., Theis, F., Tsankov, A., van den Berge, M., von Papen, M., Whitsett, J., Xavier, R., Xu, Y., Zaragosi, L.-E., and Zhang, K. (2020) SARS-CoV-2 receptor ACE2 Is an interferon-stimulated gene in human airway epithelial cells and is detected in specific cell subsets across tissues. *Cell 181* (5), 1016−1035 (e19)..
(85) Hou, Y. J., Okuda, K., Edwards, C. E., Martinez, D. R., Asakura, T., Dinnon, K. H., 3rd, Kato, T., Lee, R. E., Yount, B. L., Mascenik, T. M., Chen, G., Olivier, K. N., Ghio, A., Tse, L. V., Leist, S. R., Gralinski, L. E., Schäfer, A., Dang, H., Gilmore, R., Nakano, S., Sun, L., Fulcher, M. L., Livraghi-Butrico, A., Nicely, N. I., Cameron, M., Cameron, C., Kelvin, D. J., de Silva, A., Margolis, D. M., Markmann, A., Bartelt, L., Zumwalt, R., Martinez, F. J., Salvatore, S. P., Borczuk, A., Tata, P. R., Sontake, V., Kimple, A., Jaspers, I., O'Neal, W. K., Randell, S. H., Boucher, R. C., and Baric, R. S. (2020) SARS-CoV-2 reverse genetics reveals a variable infection gradient in the respiratory tract. *Cell 182* (2), 429−446 (e14)..
(86) Lee, J. J., Kopetz, S., Vilar, E., Shen, J. P., Chen, K., and Maitra, A. (2020) Relative abundance of SARS-CoV-2 entry genes in the enterocytes of the lower gastrointestinal tract. *Genes 11* (6), 645.
(87) Qi, F., Qian, S., Zhang, S., and Zhang, Z. (2020) Single cell RNA sequencing of 13 human tissues identify cell types and receptors of human coronaviruses. *Biochem. Biophys. Res. Commun. 526* (1), 135−140.
(88) Chai, X., Hu, L., Zhang, Y., Han, W., Lu, Z., Ke, A., Zhou, J., Shi, G., Fang, N., Fan, J., Cai, J., Fan, J., and Lan, F. (2020) Specific ACE2 expression in cholangiocytes may cause liver damage after 2019-nCoV infection. *bioRxiv* DOI: 10.1101/2020.02.03.931766.
(89) Tabibian, J. H., and LaRusso, N. F. (2014) Liver and bile. *Reference Module in Biomedical Sciences*, Elsevier.
(90) Radisic, M., Park, H., and Vunjak-Novakovic, G. (2007) Chapter Thirty-Eight - Cardiac-tissue engineering. In *Principles of Tissue Engineering* (Lanza, R., Langer, R., and Vacanti, J., Eds.) 3rd ed., pp 551−567, Academic Press, Burlington.
(91) Guo, J., Wei, X., Li, Q., Li, L., Yang, Z., Shi, Y., Qin, Y., Zhang, X., Wang, X., Zhi, X., and Meng, D. (2020) Single-cell RNA analysis on ACE2 expression provides insights into SARS-CoV-2 potential entry into the bloodstream and heart injury. *J. Cell. Physiol. 235* (12), 9884−9894.
(92) Lin, W., Hu, L., Zhang, Y., Ooi, J. D., Meng, T., Jin, P., Ding, X., Peng, L., Song, L., Xiao, Z., Ao, X., Xiao, X., Zhou, Q., Xiao, P., Fan, J., and Zhong, Y. (2020) Single-cell analysis of ACE2 expression in human kidneys and bladders reveals a potential route of 2019-nCoV infection. *bioRxiv* DOI: 10.1101/2020.02.08.939892.
(93) Chen, R., Wang, K., Yu, J., Howard, D., French, L., Chen, Z., Wen, C., and Xu, Z. (2020) The spatial and cell-type distribution of SARS-CoV-2 receptor ACE2 in human and mouse brain. *bioRxiv* DOI: 10.1101/2020.04.07.030650.
(94) Valério-Gomes, B., Guimarães, D. M., Szczupak, D., and Lent, R. (2018) The absolute number of oligodendrocytes in the adult mouse brain. *Front. Neuroanat. 12*, 90.
(95) Gabrielsson, J., and Weiner, D. (2001) *Pharmacokinetic and pharmacodynamic data analysis: Concepts and applications*, CRC Press.

https://dx.doi.org/10.1021/acsptsci.0c00183
ACS Pharmacol. Transl. Sci. 2021, 4, 248−265